JGR Earth Surface

RESEARCH ARTICLE
10.1029/2022JF006853

Strongly Depth-Dependent Ice Fabric in a Fast-Flowing Antarctic Ice Stream Revealed With Icequake Observations

S.-K. Kufner[1,2], J. Wookey[3], A. M. Brisbourne[1], C. Martín[1], T. S. Hudson[4], J. M. Kendall[4], and A. M. Smith[1]

[1]British Antarctic Survey, Natural Environment Research Council, Cambridge, UK, [2]Now at the Karlsruhe Institute of Technology, Geophysical Institute, Karlsruhe, Germany, [3]School of Earth Sciences, University of Bristol, Bristol, UK, [4]Department of Earth Sciences, University of Oxford, Oxford, UK

Key Points:

- Split shear-waves from basal microseismicity are used to invert for ice fabric
- The preferred model has three depth layers of distinct fabric including a tilted cone, thick girdle, and vertical cone
- Ice viscosity varies with depth, direction, and component of deformation, with significant implications for ice deformation

Supporting Information:

Supporting Information may be found in the online version of this article.

Correspondence to:

S.-K. Kufner,
sofia-katerina.kufner@kit.edu

Citation:

Kufner, S.-K., Wookey, J., Brisbourne, A. M., Martín, C., Hudson, T. S., Kendall, J. M., & Smith, A. M. (2023). Strongly depth-dependent ice fabric in a fast-flowing Antarctic ice stream revealed with icequake observations. *Journal of Geophysical Research: Earth Surface*, *128*, e2022JF006853. https://doi.org/10.1029/2022JF006853

Received 21 JUL 2022
Accepted 2 MAR 2023

Abstract The crystal orientation fabric of glacier ice impacts its strength and flow. Crystal fabric is therefore an important consideration when modeling ice flow. Here, we show that shear-wave splitting (SWS) measured with glacial microseismicity can be used to invert seismic anisotropy and ice fabric, if represented in a statistical sense. Rutford Ice Stream (RIS) is a fast-flowing Antarctic ice stream, a setting crucial for informing large-scale ice sheet models. We present >200,000 SWS measurements from glacial microseismicity, registered at a 38-station seismic network located ~40 km upstream of the grounding line. A representative subset of these data is inverted for ice fabric. Due to the character of SWS, which accumulates along the raypath, we include information on the depth structure from radar measurements. We find that the following three-layer configuration fits the data best: a broad vertical cone fabric near the base of RIS (500 m thick), a thick vertical girdle fabric, orientated perpendicular to flow, in the middle (1,200 m thick), and a tilted cone fabric in the uppermost 400 m. Such a variation of fabric implies a depth-dependent strength profile of the ice with the middle layer being ~3.5 times harder to deform along flow than across flow. At the same time, the middle layer is a factor ~16 softer to shear than to compression or extension along flow. If such a configuration is representative for fast-flowing ice streams, it would call for a more complex integration of viscosity in ice sheet models.

Plain Language Summary We introduce a method to derive information on the ice viscosity of a >2 km thick Antarctic Ice Stream using very small earthquakes, which are created as the ice stream flows over its bed. When ice flows, the individual ice crystals rearrange in a specific configuration. This configuration can vary, depending on the direction of applied force, making the bulk ice harder or easier to deform. This behavior can be expressed through a variable, the ice viscosity. Here, we use the recordings of icequakes recorded at seismic stations on top of the ice to infer the configuration of ice crystals and through further mathematical calculations, the viscosity between the ice-bed and the surface. Our results show that the crystal configuration and viscosity vary with depth, which severely affects the ice stream's behavior upon deformation. Such a behavior is so far not included in many numerical models which simulate the large-scale behavior of ice streams.

1. Introduction

Much of the uncertainty in current scenarios of future sea level rise originates from different predictions for the contribution of the West Antarctic Ice Sheet (IPCC, 2021). West Antarctica's contribution is mostly constrained by large-scale ice sheet models, which are designed to understand the ice sheet behavior in response to external forces (Graham et al., 2018). An essential part of such models are flow relations, which relate applied stress to the deformation in the ice. Stress modifies the internal structure of glacial ice through the alignment of individual anisotropic ice crystals into crystallographic preferred orientation (CPO) fabric (e.g., Faria et al., 2014b). The CPO fabric, also known as crystal orientation fabric in glaciology, hereafter referred to as fabric, then influences the mechanical properties, and therefore ultimately the flow pattern of ice streams, as different types of ice fabric deform distinctly under stress (Alley, 1988). At the same time, depending on the deformation kinematics, different types of ice fabric can develop.

The ice fabric can be described through the orientation of the ice-crystals' c-axes. Ice crystals are configured in layers of hexagonal rings. The normal to these rings is the c-axis (e.g., Duval et al., 1983). The c-axes tend to

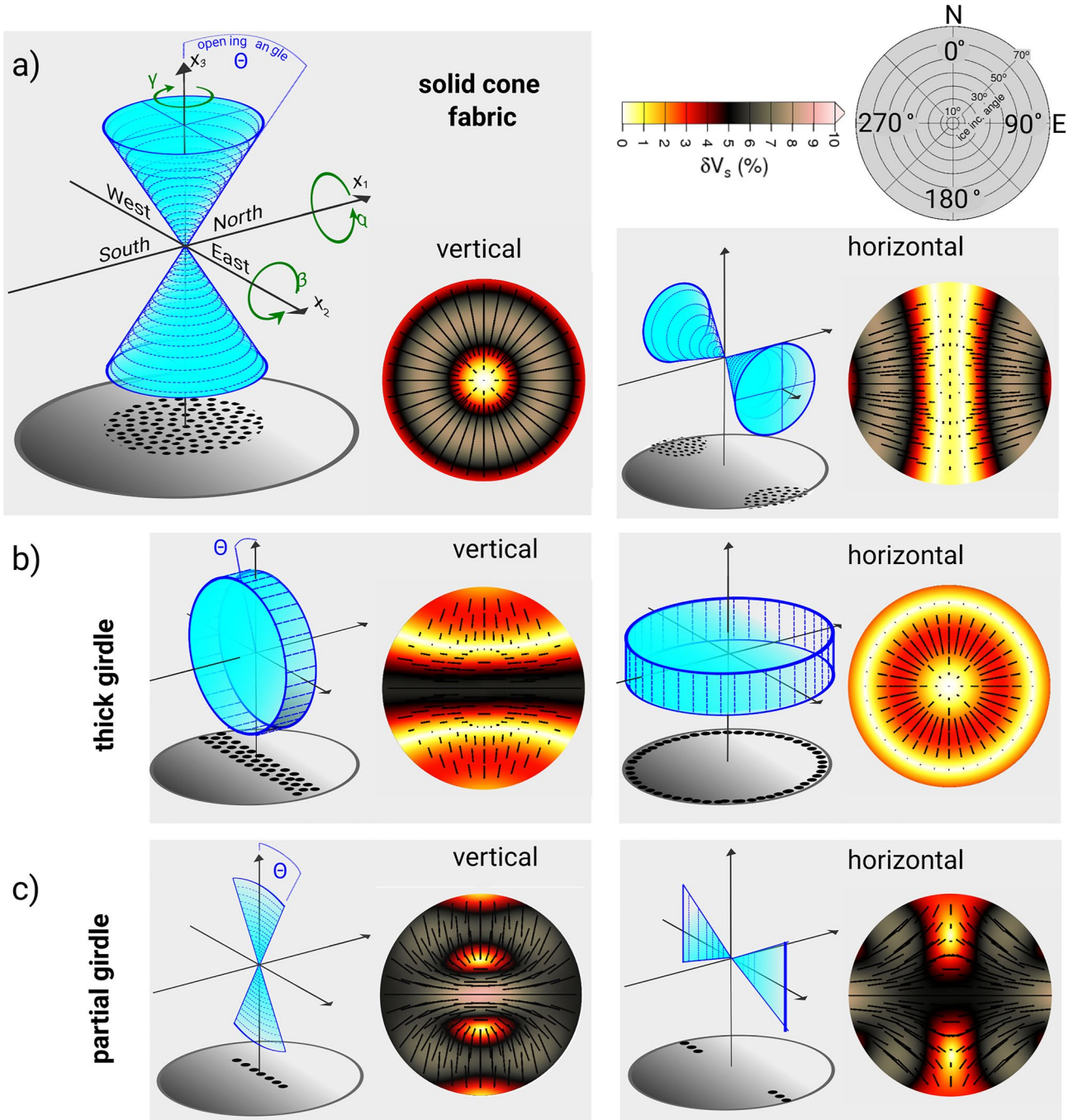

Figure 1. Schematic plots of ice fabric properties and expected shear-wave splitting pattern on a polar diagram. Note that these fabric distributions, which are used in this study, represent ice fabric in a statistical sense. Fabric figures are adapted from Maurel et al. (2015) and E. C. Smith et al. (2017). In the schematic diagrams, the envelope of c-axes is highlighted in blue, while black circles at the base of the plot show the c-axes distribution on an upper hemispheric plot. Θ describes the opening angle of the envelope, while α, β and γ are the rotation angles around the coordinate axes, as used in the inversion (see Section 4). Insets show upper hemisphere polar diagrams of the percentage of shear-wave anisotropy (δV_S), expected for the different fabric types. The associated coordinate system is given in the top right. North refers to an azimuth of 0°. (a) Vertical ($\alpha = 0°$; left) and horizontal ($\alpha = 90°$; right) solid cone fabric with $\Theta = 30°$. (b) Vertical ($\beta = 0°$; left) and horizontal ($\beta = 90°$; right) thick girdle fabric with $\Theta = 15°$. (c) Vertical ($\alpha = 0°$; left) and horizontal ($\alpha = 90°$; right) partial girdle fabric with $\Theta = 15°$.

rotate away from the direction of extension and toward the direction of compression. For example, if ice crystals are subject to uniaxial compression, their c-axes orient into a cone-shaped distribution around the direction of applied compression, commonly referred to as "cone fabric" (Figure 1a, which shows the case of a solid cone). Another mechanism to yield a cone fabric is through shearing (e.g., Qi et al., 2019). Uniaxial extension

results in "thick girdle fabric," where c-axes are oriented perpendicular to the compression axis (Figure 1b) (Alley, 1988; Maurel et al., 2015). A "partial girdle" fabric may develop under a combination of pure and simple shear (Figure 1c) (Alley, 1988; Maurel et al., 2015). In addition, there are other factors, on top of the basal plane rotation, that can affect fabric, such as temperature, and the magnitude of stress or strain (Fan et al., 2020; Qi et al., 2019). Most of these different ice fabric types induce a characteristic pattern of anisotropy (the variation of elastic or electromagnetic wave speed with direction of propagation), which is different from single-crystal ice, and which varies dependent on the azimuth and incidence angle over which the fabric is sampled (Figure 1). Laboratory and field studies have shown that the anisotropy of ice significantly influences ice deformation and should therefore be incorporated into ice sheet models (Graham et al. (2018) and references therein). Knowledge of the present-day ice fabric is therefore essential for predicting the future behavior of ice streams when using flow models (Azuma & Goto-Azuma, 1996).

Commonly, anisotropy is implemented in ice sheet models through a tensional relationship for bulk ice viscosity (Faria et al., 2014b; Gagliardini et al., 2009; Ma et al., 2010) or as a parameter, determined empirically from the surface stress field (Budd et al., 2013; Graham et al., 2018). This is because direct observations of ice fabric from drilling or coring are mostly located near ice domes (Faria et al., 2014a, 2014b), where cone fabrics, which are vertically transversely isotropic and can therefore be described through simple flow relations, are common. However, recent measurements from Rutford ice stream (RIS), a fast-flowing West Antarctic ice stream, conducted using noninvasive geophysical methods, suggest that ice fabric, and thus anisotropy is highly variable, both spatially and in depth, in such settings (Jordan et al., 2022; E. C. Smith et al., 2017). These results call for a more complex consideration of anisotropy in ice sheet models.

Noninvasive geophysical methods, like active and passive seismic imaging, or radar sounding (Harland et al., 2013; Jordan et al., 2022; Picotti et al., 2015; E. C. Smith et al., 2017), make use of the fact that the different ice fabric types feature different patterns of anisotropy. Compared to direct observations, such methods are less time- and cost-intensive in the field but result in some ambiguity in the ice fabric inferred. The radar method used by Jordan et al. (2022), for instance, is only sensitive to CPO in the horizontal plane. Thus, only the difference in the horizontal eigenvalues of the fabric-orientation tensor can be determined. In contrast, using shear-wave splitting (SWS) of seismic waves, E. C. Smith et al. (2017) were able to determine two fabric types in the ice of RIS. However, they could not resolve the vertical distribution of these different fabric types as SWS integrates along the entire ray path of seismic waves (Silver & Savage, 1994), Here, we aim to obtain a more comprehensive picture of ice fabric at RIS by making use of the advantages of different geophysical methods. First, we generate SWS measurements similar to E. C. Smith et al. (2017). We then use the seismic waveforms to invert for ice fabric, implementing a multiple-layer inversion scheme (Wookey, 2012). We show that the problem of unknown distribution of fabric types can be overcome by using depth-information from radar measurements (Jordan et al., 2022) as prior constraints for the inversion. This approach allows us to isolate the depth distribution of fabric types and calculate the full viscosity tensor for these depth domains. Both these steps are essential to incorporate geophysical measurements (e.g., ice described in terms of seismic anisotropy) into ice sheet models where, for example, the viscosity tensor is a model input parameter.

2. Site Description and Data Set

Our study area is in a central section of RIS, 40 km upstream from the grounding line (Figure 2). RIS flows approximately southward into the Filchner-Ronne Ice Shelf with a velocity of 375 m/a (Adalgeirsdóttir et al., 2008). Beneath the 8×8 km 38-station seismic array (Figure 2), which was deployed as part of the BEAMISH project (A. M. Smith et al., 2020), the ice thickness is approximately 2.2 km (King et al., 2016). Ice flow direction, determined from the GPS instruments attached to our seismometers, is 148° relative to True North. Due to the movement of the ice over its bed, many microearthquakes (local magnitude smaller than −0.3) are created in this section of RIS at the ice-bed interface (Kufner et al., 2021; E. C. Smith et al., 2015). These events are characterized by relatively simple waveforms, featuring an impulsive P-wave onset with 10–200 Hz frequency followed by a shear-wave with frequencies between 30 and 100 Hz (Kufner et al., 2021). In addition, shear-wave splitting (SWS; e.g., Savage, 1999) is observed. This phenomenon arises if the initial polarization of a shear-wave is not parallel to the anisotropic axis of symmetry in a specific medium. In this case, the shear-wave is split into two orthogonally polarized quasi shear-waves (e.g., Savage, 1999, Figure 3). The quasi shear-waves travel at different speeds, dependent on the ray path orientation relative to the ice fabric. The delay time (dt) between the two

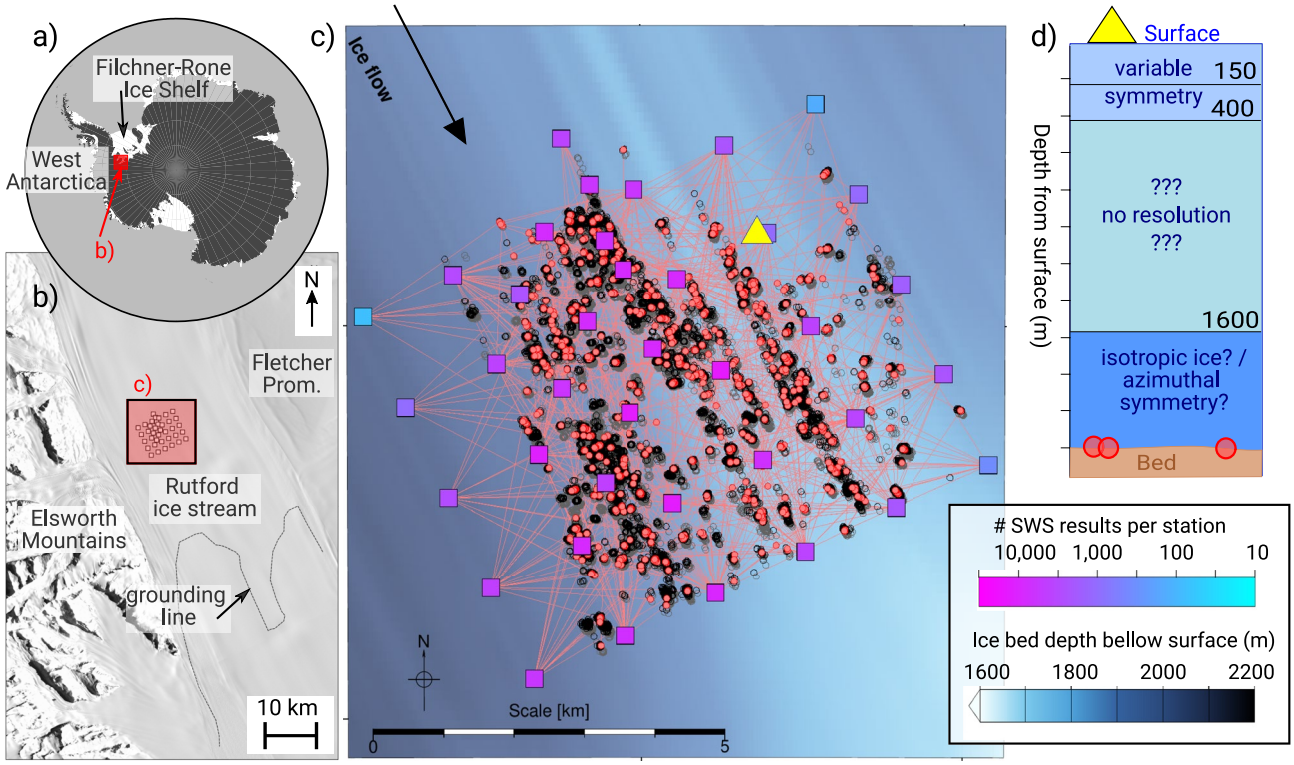

Figure 2. Geographic setting of Rutford Ice Stream (RIS), location of seismic array and earthquake locations used for shear-wave splitting (SWS) analysis. (a) Location of RIS on the Antarctic continent. (b) Overview map of RIS with the LIMA image in the background (USGS, 2007). Plot range is 77.852°S/82.528°W (upper right corner) to 78.710°S/85.236°W (lower left corner). (c) Zoom into the study site. The yellow triangle shows the radar survey site of Jordan et al. (2022) used to design input ice fabric configurations for inversion. Seismic stations (squares) are color coded logarithmically according to the number of good SWS results registered at the station. Gray circles are all microearthquakes on which SWS was performed (167,262 events), black circles are those with good SWS results (69,629 events), and red circles and light red ray paths highlight those selected for ice fabric inversion (1090 events). The background color scale shows the ice bed depth relative to the surface (King et al., 2016). (d) Schematic sketch through a depth-profile of RIS, illustrating the radar results of Jordan et al. (2022) and the icequake location (red circles) at the ice-bed interface.

shear-wave components is an indicator of the strength of seismic anisotropy along the ray path, the polarization direction of the quasi-shear-waves depends on the symmetry of anisotropy along the ray path (e.g., Silver & Chan, 1991; Savage, 1999; Teanby et al., 2004).

Here, we measure *dt* and Φ (the polarization direction of the faster of the two quasi-shear-waves) from 69,629 microearthquakes (Figure 2) recorded at 38 seismometers during approximately three months from November 2018 to February 2019. Waveforms were recorded with a sampling frequency of 1,000 Hz on Reftek RT-130 data loggers with 4.5 Hz three-component geophones (see Kufner et al. (2021) for details). The event-station pairs used in this study have been selected from the event catalog of Kufner et al. (2021), based on the availability of both P- and S-picks and a focal mechanism solution; the latter allowed us to compare the slip vector from focal mechanisms and SWS as an additional quality control.

Previously, E. C. Smith et al. (2017) used a 10-station seismic array at a similar location to detect the SWS of 5,951 event-station pairs and to invert the SWS parameters for ice fabric. E. C. Smith et al. (2017) tested combinations of two different fabric types (hereafter referred to as "mixed" fabric) as potential candidates that could create the observed SWS pattern. They concluded that the anisotropy observed in their SWS data could be due to a horizontal partial girdle, orientated with a symmetry axis perpendicular to ice flow, combined with a solid cone fabric with a relatively large opening angle of 73° (see Figure 1 for a schematic sketch of different ice fabric geometries). However, E. C. Smith et al. (2017) noted that the inversion for mixed fabric is unconstrained as SWS samples the anisotropy along the entire ray path. Thus, the two fabric types may be spatially separated in the ice stream. Their observations indicate a region of mostly extension and horizontal confinement (expressed through the horizontal partial girdle) in combination with a weakly anisotropic region (expressed through the cone with a large opening angle). The weakly anisotropic region could either be the firn layer or a deeper region with thin

layering, which would weaken the bulk anisotropy. It was later noted that a horizontal partial girdle fabric has never been observed directly in ice core samples (Lutz et al., 2020) or in ice deformation experiments (e.g., Richards et al., 2021). Thus, although the E. C. Smith et al. (2017)-model explains the SWS data, it remains a topic of discussion if this configuration is a realistic scenario in a fast-flowing ice stream. SWS results similar to E. C. Smith et al. (2017) were also obtained by Harland et al. (2013), calculating SWS at a site closer to the grounding line, using five seismic stations. They similarly measured an alignment of fast directions parallel to ice-flow and concluded that a cone as well as some horizontally transversely isotropic fabric (e.g., a girdle) would be needed to explain these results.

A more recent polarimetric radar study by Jordan et al. (2022) delineated the shallow depth structure of ice fabric at RIS in more detail. At a site towards the edge of the seismic array used in this study (site A1 in Jordan et al. (2022); see Figure 2), the azimuthal anisotropy was observed to change with depth in the upper 400 m, with a symmetry axis within ±20° of the current flow direction of RIS. In the upper ∼150 m, the azimuthal fabric anisotropy is orientated closely with the surface strain field, whereas the symmetry axes in a deeper (150–400 m) layer appeared rotated by ∼20° in a clockwise direction relative to shallower ice. The surface strain rate was calculated by Jordan et al. (2022) using satellite data. The section of RIS in which our study region is located is characterized by small along-flow compression and small lateral extension relative to flow. By contrast, further upstream, along-flow extension is more dominant. Thus, Jordan et al. (2022) suggested that the ice fabric configuration they measure at site A1 might arise as the fabric is created further upstream and then buried and advected. However, due to the radar survey method, only azimuthal anisotropy can be observed. For example, a thick girdle or a horizontally oriented cone fabric would yield the same pattern in the radar data. At greater depth (∼400–1,600 m), the method used by Jordan et al. (2022) did not have sufficient coherence in the data to detect the axes of anisotropy. Notably, coherence does improve deeper than 1,600 m and a region with azimuthally invariant anisotropy was inferred. This suggests either isotropic ice or a fabric with a vertical axis of symmetry at depth. Furthermore, the sharp recovery of coherence at these greater depths could indicate that the ice fabric from 400 to 1,600 m depth differs from that in the deepest ice (see sketch in Figure 2d).

The combination of results from E. C. Smith et al. (2017) and Jordan et al. (2022) suggests that the ice fabric of RIS is depth-dependent and three or more discrete layers of distinct ice fabric may exist. Intensity and fabric types in these layers were inferred through the studies of E. C. Smith et al. (2017) and Jordan et al. (2022) but could not be uniquely defined. In this study, we extend the seismic anisotropy study of E. C. Smith et al. (2017), making use of the results from Jordan et al. (2022), to obtain a more comprehensive picture of the variation of ice fabric with depth, which then allows us to calculate the full fabric orientation tensor and ice viscosity.

3. Shear-Wave Splitting

3.1. Method and Data Processing

To calculate SWS parameters from our waveform data, preprocessing includes filtering and downsampling. Seismograms are filtered between 8 and 125 Hz, using a two-pole Butterworth filter, and downsampled from 1,000 to 500 Hz. Filtering increases the number of high-quality splitting measurements at larger epicentral distances, while leaving results at smaller epicentral distances unchanged compared to the measurements using the raw data. Downsampling increases processing speed, whilst preserving the frequencies of interest.

We use the MFAST software (Savage et al., 2010) for SWS analysis. MFAST implements a minimum eigenvalue analysis algorithm (Silver & Chan, 1991) to calculate SWS in multiple time windows around a specified S-wave onset. For each of these measurement windows, inverse splitting parameters (i.e., a rotation to the fast-slow reference frame, followed by a time-shift) are applied to the horizontal waveforms, in accordance with Savage et al. (2010), based on the assumptions that most of the S-energy is recorded on the horizontal components. This aims to find the combination of splitting parameters that minimizes the following expression, composed of the two eigenvalues (λ_1 and λ_2) of the covariance matrix of the two horizontal traces:

$$\lambda_2' = (\lambda_2 / \lambda_1) * \lambda_2 \quad (1)$$

Prior to SWS calculation, the mean of the two traces is removed, which stabilizes the solution. In addition to the two splitting parameters (Φ and dt), a by-product of the minimum eigenvalue method is the initial polarization direction (which depends on the source moment tensor). The SWS measurement is then repeated for different

analysis windows, which differ slightly relative to the S-onset. The final splitting parameters for a specific event are then determined as the most stable set of splitting parameters from these individual measurements (see Teanby et al. (2004) for more details). In MFAST, the start and end points of the measurement windows are variable, dependent on an event's dominant frequency. Formal errors in the measured Φ and *dt* are estimated using the *F*-test approach (Silver & Chan, 1991; Walsh et al., 2013).

Here, we first calculate the signal-to-noise (SNR) ratio of all candidate events based on time windows 0.1 s prior to and after the S-onset on the horizontal components and require a minimum SNR of two to proceed with the analysis. In the case where half the S-P time is smaller than 0.1 s, we restrict the noise window to half the S-P time. We search Φ from 0 to 180° and dt from 0 to 0.1 s, based on trial runs with the largest possible *dt*. We find our SWS results to be remarkably stable across different analysis windows as glacial microseismicity at RIS features waveforms that are in general less complex than those of tectonic earthquakes. We therefore use only two analysis time windows prior to, and four after, the S-onset, which increases the processing speed by a factor of ∼10 compared to the default settings in MFAST. Given the large number of events, this step was essential to reduce computational power requirements. However, if the cluster analysis was not able to find a stable solution with the settings described above, we re-run the measurement and increased the number of measurement windows prior to the S-onset to six. In addition, the same restriction criteria for the SNR analysis are implemented, so that P-wave energy is never included in the analysis. For our final set of SWS results, measurement windows range from 0.013 to 1.25 s prior and 0.050–1.01 s after the S-onset, while the mean dominant frequency is 29 Hz. After applying the MFAST algorithm to the data but prior to quality control, we obtain 705,441 sets of splitting parameters from the initial 989,686 event-station pairs. For the event-station pairs for which no stable solution was found, ∼95% were rejected due to low signal amplitude on the traces. For the remaining ∼5% of rejected results, no stable cluster could be found. This occurs when there is interference in the wavelet or when the bandwidth of the signal is limited. Depending on the stability of the cluster and the error range of the final splitting parameters, MFAST adds a quality grade to the data (see details in Savage et al. (2010)). Here, we use these grades for reference but additionally apply data set specific quality restrictions to our final splitting measurements. These criteria have been defined based on visual inspection of a subset of results. We require the calculated error in Φ to be smaller than 15° and the error in dt to be smaller than 0.005 s. Furthermore, a quality criterion is defined based on two parameters: (a) the amplitude ratio on the component which is normal to the initial source polarization direction (component p⊥; see Figure 3), after and before correcting for splitting (termed stc/sto; equivalent to "amplitude **st**ream **c**orrected" divided by "amplitude **st**ream **o**riginal"); (b) the cross-correlation coefficient (coeff) of the fast and slow shear-waves after correcting for splitting. An event was accepted if one of the following three criteria was applied: (stc/sto < 0.6 and coeff > 0.7) or (stc/sto < 0.5 and coeff > 0.6) or (stc/sto < 0.45 and coeff > 0.5). These criteria were determined from a visual inspection of a subset of the data. For example, by applying these criteria, events where waveforms are correlated with noise, or where splitting is not removed sufficiently, are excluded. These criteria represent a more visual description of how effectively λ_2 is minimized. In the idealized case of near-zero λ_2, coeff would be 1 and stc/sto would be 0.

Figure 3 shows examples of two SWS measurements, one high-quality result (Figure 3a; SNR 14.7) and a second example of lower quality (Figure 3b; SNR 9.1). SWS is successfully measured and removed in the first case. By contrast, the cross-correlation coefficient between the corrected fast and slow components in the second case is smaller and the maximum in the misfit surface of $1/\lambda_2$' is less pronounced. Notably, the lower quality of the second example is not due to noise but due to the shape of the waveforms themselves. In addition, we tested whether our results depend on filter frequency but found no correlation within the frequency range considered here (see details in Text S1, Figures S1 and S2 in Supporting Information S1).

3.2. Shear-Wave Splitting Results

We obtained 202,651 SWS results (average: 5,333/min.:74/max.:13,677 results per station; average:3/min.:1/max.:16 results per event) from the initial 989,686 event-station pairs. The data set is available online (Kufner et al., 2022). The distribution of these results in the map view (Figure 2) is representative of the available event and station distribution (i.e., apparent clustering of good splitting results in the center of the network, due to more available rays and microearthquakes). Results are presented in Figure 4 on a polar plot in upper hemispheric projection, although many individual SWS results overlap in this representation. Therefore, we additionally calculated bin-wise averages (Figure 5; see Figure S3 in Supporting Information S1 for the weighting

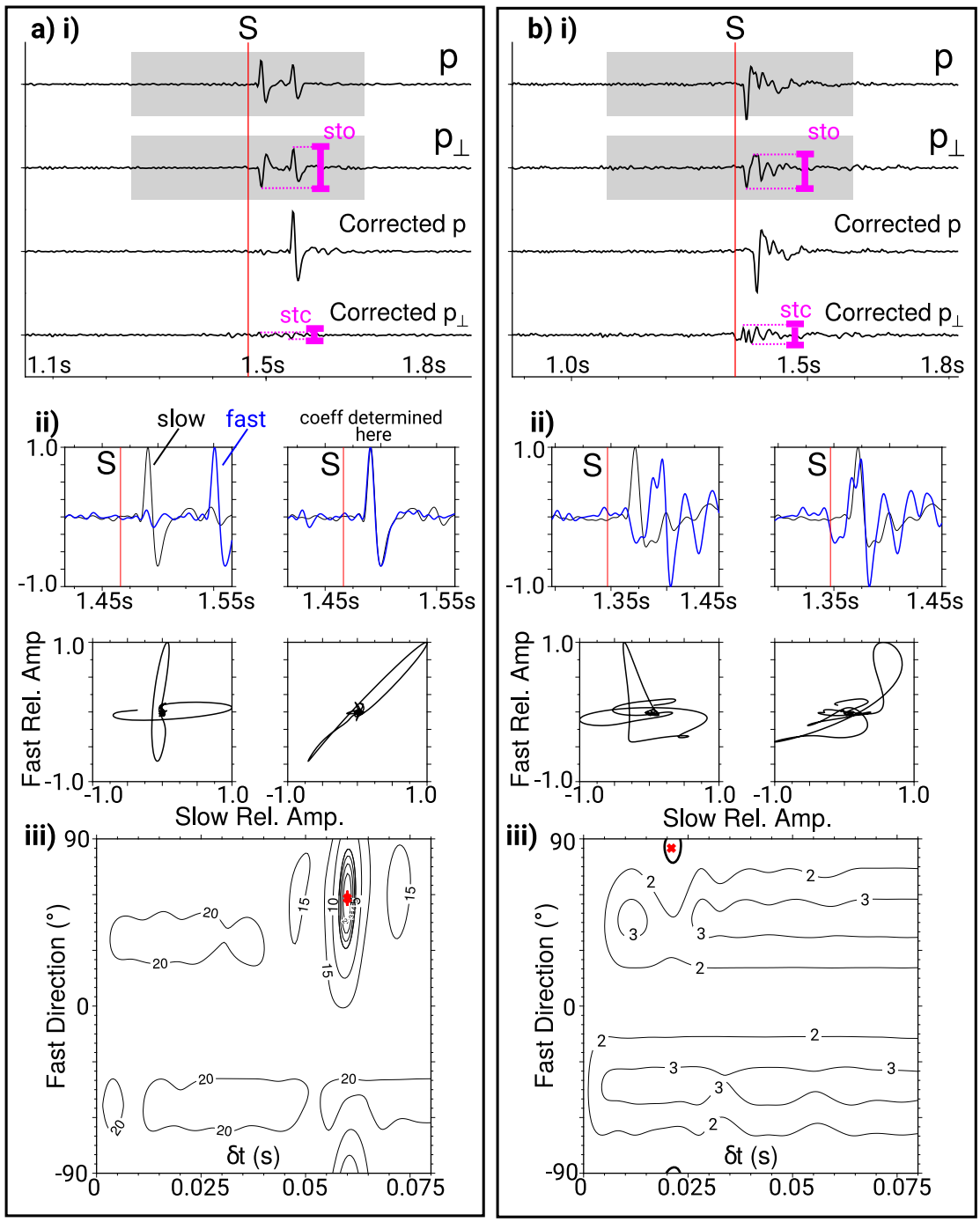

Figure 3.

function), which helps identify trends in the data. Here, and in the following analysis, we use the percentage of anisotropy (δV_S)—the percentage of shear-wave variation from the average isotropic shear-wave velocity (V_S = 1,944 m s^{-1})—instead of dt when visualizing SWS results. δV_S is calculated as follows:

$$\delta V_S = 100 * (V_S * dt)/r \quad (2)$$

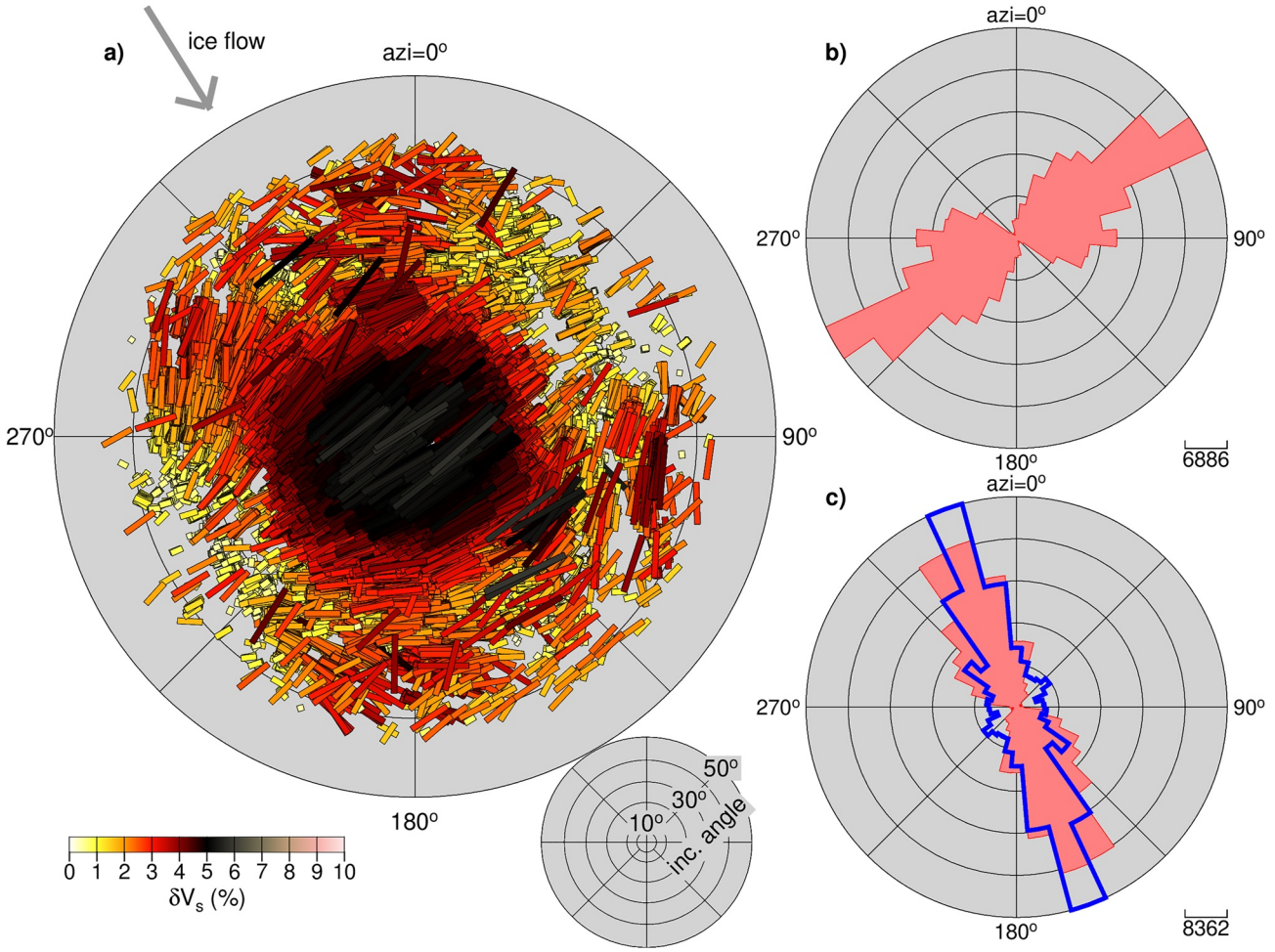

Figure 4. (a) Upper hemisphere plot of shear-wave splitting (SWS) measurements. Direction of bars indicates Φ, length and color the percentage of anisotropy (δV_S). The plot routine sorts the results by δV_S with largest δV_S being in the foreground and smallest δV_S in the background. Azimuth from event to station (azi) is plotted clockwise from north, incidence angles of the rays (inc. angles) as shown in the inset plot. Ice flow direction is drawn as a gray arrow. (b) Rose diagram of Φ, plotted in 10° bins. (c) Rose diagram comparing initial S-wave polarization determined from SWS (red) and slip vectors (Kufner et al., 2021) determined from the events' focal mechanisms (blue).

Where r is the ray length from an icequake to a seismic station, calculated from a layered velocity model with a 100 m thick firn layer overlying glacial ice, as used by Kufner et al. (2021). The advantage of δV_S is that this is normalized with respect to ray-path length, unlike dt.

Our SWS results include rays from all azimuths, epicentral distances of 0.01–4.9 km, ray path length of 2.0–5.2 km, event depths (relative to 0 elevation) from 1.6 to 2.2 km and incidence angles from 1.2 to 42.9°. Due to the strong near-surface velocity gradient, few of the incidence angles exceed 35°. For larger incidence angles,

Figure 3. Examples for shear-wave splitting (SWS) results. Subfigures (i) show the horizontal traces rotated parallel (p) and perpendicular (p⊥) to the polarization direction, which is determined in MFAST together with the splitting parameters. "Corrected" refers to traces rotated into and perpendicular to the polarization direction after correction for the optimum anisotropy parameters. Amplitudes of the traces are normalized. The analysis window is highlighted in gray and the S-pick time in red. Time is relative to the start of the data trace. For an optimum set of splitting parameters, the energy on "corrected p⊥" is minimized. Subfigures (ii) show waveforms (top) and particle motion (bottom) of the fast and slow components. Original fast and slow waveforms are plotted in the two left panels, while anisotropy-corrected waveforms are plotted in the two right panels. As in (i), the red line represents the S-pick. Subfigures iii show the misfit surface of λ_2'. Contours are scaled relative to the eigenvalues of the covariance matrix of the best measurement. The 95% confidence interval corresponds to the bold "mixed" contour. Other contours demarcate multiples of the 95% confidence interval. This means that a small range of values (see e.g., difference in (a)iii and (b)iii) indicates that the best and the worst results do not differ much. The optimal splitting parameters are highlighted with a red cross. (a) Example for high-quality results, representative for events with near vertical incidence angle (event date time: 2019/021/01 01:01:17; magnitude: −1.15; epicentral distance: 0.14 km; azimuth: 137°; incidence angle: 5°). Here, stc/sto = 0.163 and coeff = 0.95 (see Section 3.1 for the description of these quality parameters). (b) Example of a result with worse quality (stc/sto = 0.486 and coeff = 0.61). For instance, the final SWS parameter does not completely remove the energy on the "corrected p⊥" component (event date time: 2019/01/01 00:18:09; magnitude: −0.79; epicentral distance: 1.72 km; azimuth: 352°; incidence angle: 26°). Such results mostly occur at larger incidence angles but not for all azimuths.

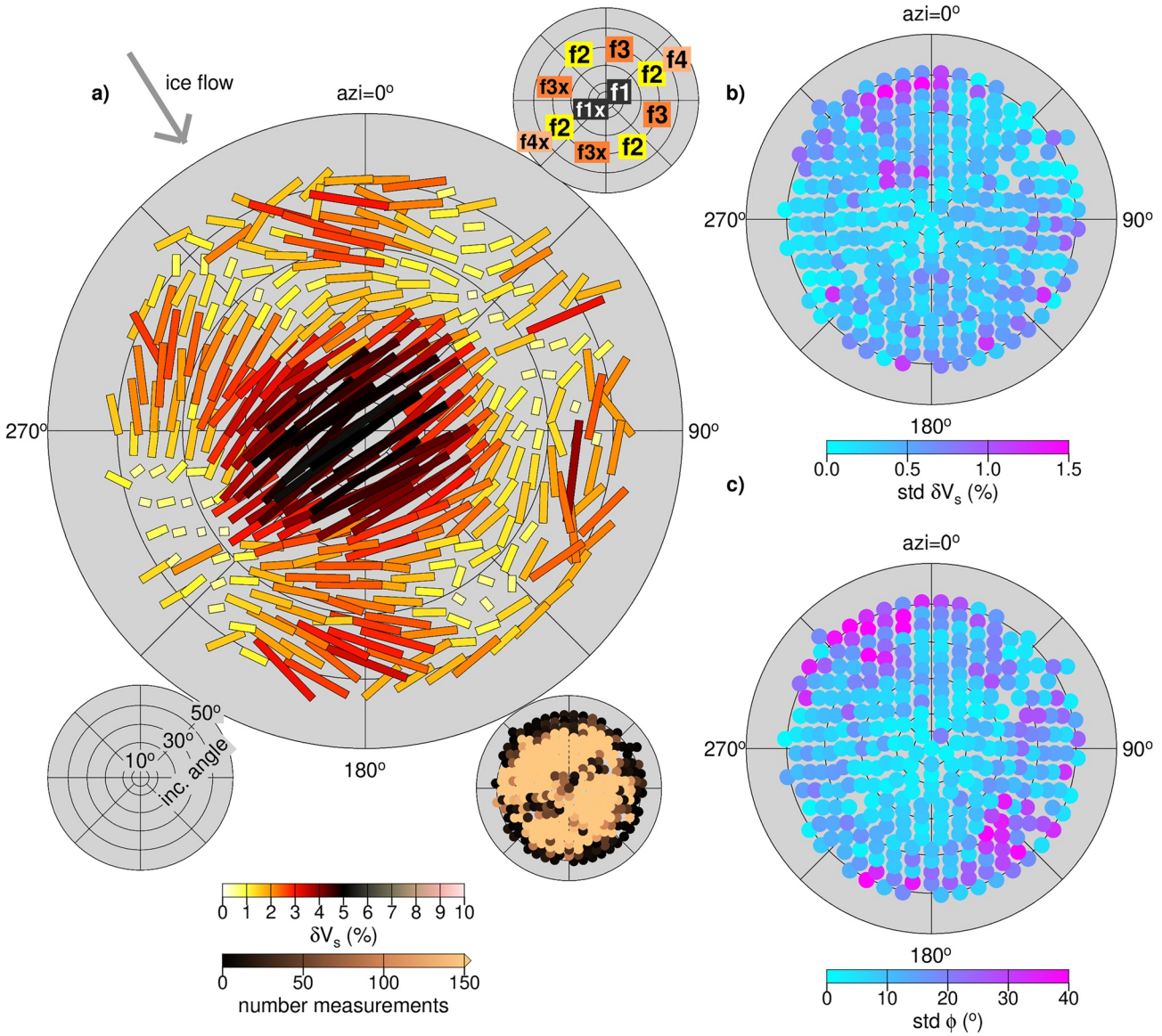

Figure 5. (a) Upper hemisphere plot of averaged shear-wave splitting measurements. Averaging is performed on bins of 3° incident angle. Azimuthal bins are adjusted dependent on the incidence angle, with one bin at an incidence angle of 0° and 48° bins at an incidence angle of 40°. In each bin, weighted averages are calculated based on the events' signal-to-noise ratio (see Figure S3 in Supporting Information S1 for the weighting function) and only splitting results with ACl quality from MFAST are included. Bottom inset shows the number of measurements included in each bin. The color scale is clipped to highlight bins with few measurements. The maximum number of measurements per bin is 5513, the mean is 531. Top inset shows labels of the main features in the data as discussed in Section 3.2. (b, c) Upper hemisphere plot of standard deviation (std) of δV_S and Φ per bin.

P-wave conversions may bias the SWS results (Crampin & Lovell, 1991; Paulssen, 2004). However, as the general trend of the SWS results is consistent between 30° and 43°, this set of results seems unaffected by such a bias.

The initial shear-wave polarization determined from SWS (average of 154°) and the slip vectors from focal mechanisms, determined from the fault plane solutions of Kufner et al. (2021) (average of 160°), are comparable (Figure 4c). As these two measures are determined independently, their similarity validates the quality of the SWS parameters. Lastly, Figures 5b and 5c show the standard deviation (σ) of splitting parameters from the bin-wise averaged values. σ is small (average σ of δV_S: 0.49%; average σ of Φ: 15.7°), which suggests a general consistency in the results throughout the study region.

Average δV_S is 2.2% (min./max.: 0.16/6.6%), which is calculated from split times between 0.0025 and 0.084 s (average: 0.029 s; average error: 0.00038 s). Average Φ is 61° (average error: 3.8°). We note that this average

Φ is nearly perpendicular to the initial polarization of the shear-waves. Nevertheless, we obtain good splitting results as icequake-waveforms are extremely simple and the anisotropy percentage is relatively high compared to many tectonic settings. SWS parameters strongly vary with azimuth and incidence angle (Figures 4 and 5). Φ is predominantly perpendicular to the ice flow direction. The highest δV_S values (up to 6.6%) are measured for incidence angles smaller than ∼15° (highlighted as feature f1/f1x in Figure 5a; please see the next paragraph, where small-scale trends in the data are described, for the explanation of difference in f1 and f1x). At incidence angles between ∼15° and ∼30°, δV_S is smaller and alternates in magnitude dependent on azimuth. The smallest δV_S values (<1%) are measured in four domains centered around ∼48° (spanning the azimuthal range from 20° to 75°), ∼138° (from 115° to 162°), ∼240° (from 213° to 268°) and ∼322° (from 300° to 344°) (highlighted as features f2 in Figure 5a). These domains are oriented roughly parallel and perpendicular to the ice flow direction at the surface. For the other azimuthal orientations, δV_S is larger (between 2% and 4%) but Φ is rotated by approximately 20° relative to the direction perpendicular to ice flow (highlighted as feature f3/f3x in Figure 4a). For the largest incidence angles (>30°), the variations in the intensity of δV_S are less intense, and δV_S is larger (between 2% and 4%) for all azimuths (highlighted as feature f4/f4x in Figure 5a).

In addition to these large-scale trends, we resolve a modulation of the splitting results relative to the symmetry axis of ice flow direction (see also Figure S4 in Supporting Information S1 which highlights these features by plotting the results mirrored relative to the symmetry axes): First, the SWS measurements at small incidence angles are not purely perpendicular to flow but exhibit a small rotation toward this symmetry axis in the south-west (at an azimuth of ∼240°; highlighted as feature f1x in Figure 5a). Next, we observe a slight asymmetry in the intensity of the f3 domains: larger δV_S is observed in the south-west (at azimuths of ∼285 and ∼195°; highlighted as feature f3x in Figure 5a). Lastly, for the largest incidence angles (>30°), we observe larger δV_S in the south-west (highlighted as feature f4x in Figure 5a) compared to the north-east. These patterns in the data remain stable, independent of whether null measurements (15% of all measurements, for which the difference between Φ and initial polarization is <20°) are included or excluded from the polar plots (Figure S5 in Supporting Information S1). In addition, we investigate the data set for temporal and spatial changes in splitting parameters (Section S2 and Figure S6 in Supporting Information S1). We do not observe such trends, at least at a level larger than the measurement uncertainty of the SWS results. This confirms that the asymmetry in SWS results described above is a robust observation.

4. Inversion for Ice Fabric

4.1. Inversion Method

Figure 6 outlines the workflow that is used to determine which ice fabric combination would yield the seismic anisotropy pattern in Figures 4 and 5. The core of the workflow (step 2 in Figure 6) is performed by the slightly modified multiple layer SWS inversion scheme introduced by Wookey (2012). Within the inversion scheme, the subsurface is separated into several depth domains, for which a specific ice fabric is defined. For each of these depth domains, several ice fabric-specific parameters (e.g., the fabric opening angle; see details in Section 4.2) are varied over a predefined range of values (e.g., from 0 to 90°). In each layer, and for all combinations of ice fabric-specific parameters, splitting parameters (Φ and *dt*) are then calculated based on the anisotropic tensors of the fabric and the geometry of different input ray paths (incidence angle and azimuth). Elastic tensors of ice fabric are defined according to Maurel et al. (2015). The splitting parameters for each depth domain are then used to correct the waveforms through time shifts and the trace rotation. This correction is applied for all layers in reverse order, starting with the recorded waveforms in the uppermost domain and operating on the sequentially modified waveforms in the lower domains. Only the part of the waveform that the SWS measurement was derived from is used. After sequentially applying the splitting parameters of all depth domains, λ_2' is calculated from the resulting waveforms for each ray individually. λ_2' is composed of the two eigenvalues of the covariance matrix of the two horizontal traces ($(\lambda_2/\lambda_1)*\lambda_2$; see Equation 2). The aim is to obtain results comparable to MFAST, which also calculates its results by minimizing λ_2'.

The algorithm then searches for the input set of fabric-specific parameters that maximizes the inverse of the sum of λ_2' of all input waveforms ($1/\Sigma\lambda_2$'). This search for the best set of ice fabric parameters is conducted via a nonlinear inversion scheme (Markov Chain Monte-Carlo using a Metropolis-Hastings algorithm; e.g., Chib & Greenberg, 1995). The advantage of the Metropolis-Hastings algorithm is that there is no need to sample the entire parameter range with equal spacing. Instead, denser sampling is applied close to a local or global maximum in $1/\Sigma\lambda_2$'. The critical parameters that govern the inversion are the maximum number of inversion runs with different

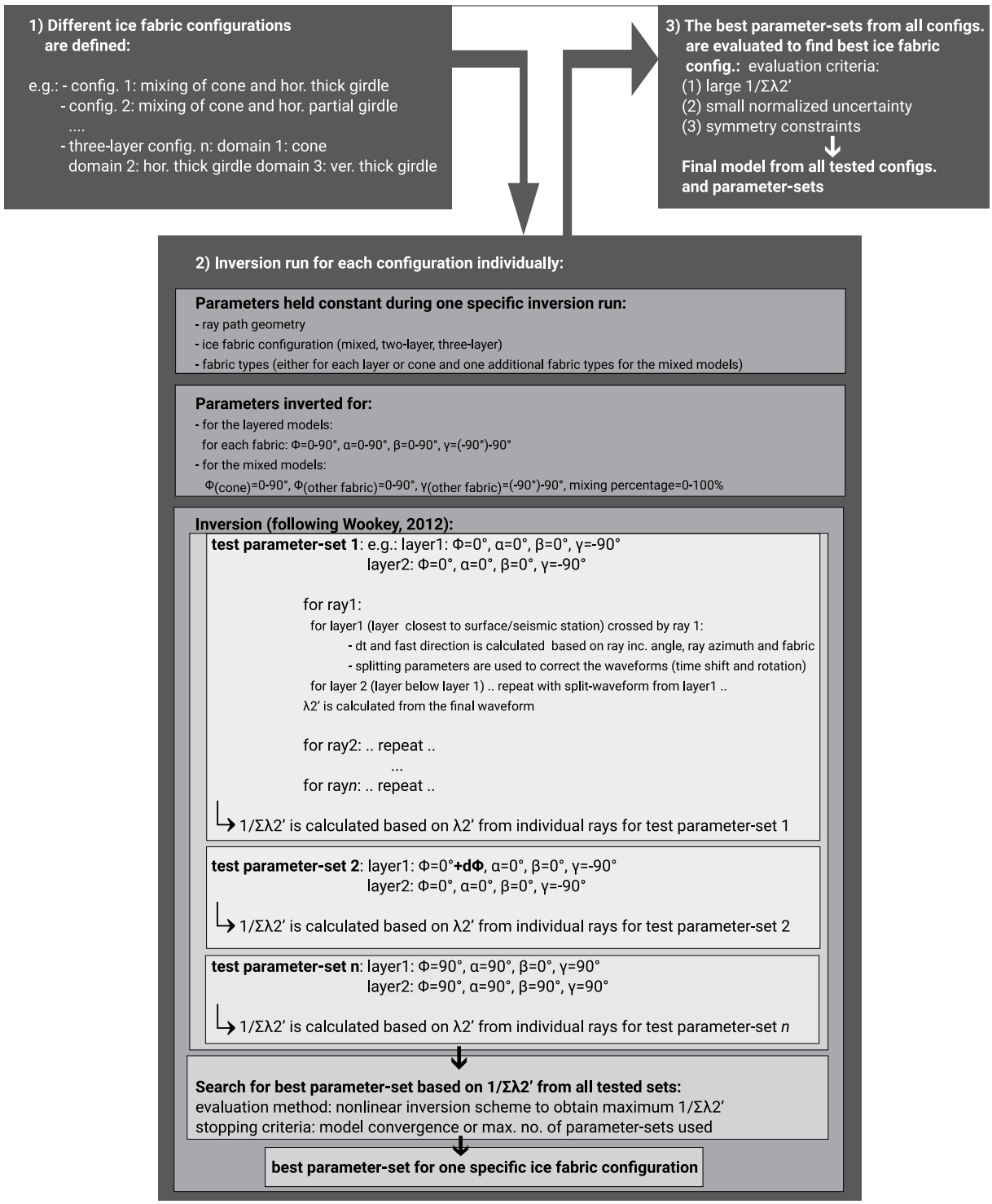

Figure 6. Schematic outline of the inversion scheme. The actual inversion for ice fabric (step 2) is performed for multiple input geometries (listed in step 1; see details in Table S1 in Supporting Information S1 for a complete and more detailed list). Based on the inversion output from the individual ice fabric configurations, and additional quality criteria, the final model is chosen (step 3). See Sections 4.1 and 4.2 for a detailed description of the workflow.

input parameters the algorithm will perform and the stopping criteria (i.e., the point when a maximum $1/\Sigma\lambda_2$' is considered as the global maximum). The stopping criteria were adapted from Wookey (2012). They were defined as the point where at least 11,000 inversion runs with small variation of fabric-specific input parameters did not yield an improvement of the maximum $1/\Sigma\lambda_2$' value within a convergence limit of 0.0005. To determine the

ideal number of inversion runs, we run initial inversions with up to 1,000,000 parameter configurations and subsequently decreased this number, while checking the inversion output (value of maximum $1/\Sigma\lambda_2$') and the number of inversion performed before the stopping criteria applied. We found that the inversion stopped after ~170,000 runs, while the inversion output remained stable down to ~100,000 runs. We therefore used 200,000 inversion runs. This means that the fabric-specific inversion parameters are sampled in the subdegree range close to the maximum of $1/\Sigma\lambda_2$'.

The uncertainty U of each ice fabric-specific parameter is defined from the range of all parameter-sets that lie in the upper 20% of the maximum $1/\Sigma\lambda_2$'. We selected this value as it yielded comparable uncertainty bounds to those derived for SWS in MFAST, when running the inversion for one ray only. For these tests, we used five rays with vertical incidence and with larger incidence angles over a range of azimuths. The uncertainty of a specific parameter-set, termed *normalized uncertainty* in the following, is defined as the normalized sum of the uncertainties of the individual parameters:

$$\text{normalized uncertainty} = (\Sigma\, U') \,/\, n \tag{3}$$

Where n is the number of free parameters in an ice fabric configuration and U' refers to the uncertainty of each individual parameter, where the parameter range was normalized to values between 0 and 1 to ensure equal weight for all parameters.

Modifications in the inversion scheme applied here, compared to the original version of Wookey (2012), include removing the mean of the waveforms when calculating the covariance matrix; using $\lambda_2' = (\lambda_2/\lambda_1)*\lambda_2$ instead of λ_2; and adapting the inversion scheme for ice fabric through implementing the elastic tensors following the formulation of Maurel et al. (2015). Adaptations were required to describe the anisotropy expected due to ice fabric attributed to the specific setting of a glacier; using λ_2' and removing the mean of the waveforms yielded more stable results in trial inversion runs and was adapted from MFAST.

4.2. Ice Fabric Configuration Setup and Determination of Final Model

During one inversion run (step 2 in Figure 6), the ice fabric configuration (e.g., the distribution of ice fabric at different depth levels) is held constant and only the parameter-set, which describes the ice fabric geometry (e.g., opening angle, orientation, etc.) is varied. As the radar results of Jordan et al. (2022) leave some freedom for interpretation regarding the distribution of ice fabric at depth, we run the inversion scheme (step 2 in Figure 6) multiple times for different ice fabric configurations (step 1 in Figure 6). The best and final model is then derived from all combinations of input ice fabric configurations and parameter-sets within these configurations (step 3 in Figure 6).

Jordan et al. (2022) resolve horizontally anisotropic fabric in the upper 400 m of RIS. At greater depth, coherency in their data decreases sharply but recovers at 1,600 m depth, where observations are consistent with a horizontally isotropic fabric. Based on these results, we define a three-layer configuration: In the upper two layers (surface to 400 m depth and 400–1,600 m depth), we test all likely fabric types (cone, thick girdle, and partial girdle). For each fabric type, we run three different configurations: in two different configurations, the fabric is fixed to be either vertical (α or $\beta = 0°$; see Figure 1 for details on fabric geometry) or horizontal (α or $\beta = 90°$). In the third configuration, we invert for α or β as well. Theoretically, this third configuration included the case of vertically or horizontally orientated fabric. However, predefining the fabric orientation reduced the number of free parameters (e.g., from 7 to 6 as one angle is held constant). We included these configurations to evaluate if reducing the number of free parameters had an impact on the results. In all these configurations, we also invert for the opening angles of the fabric and γ, which is the rotation of the fabric relative to north. The separation of the upper 1,600 m into two layers is based on the assumption that the sharp drop in the coherency of radar results may arise from a change in the ice fabric. We also include the case that the ice fabric remained stable by inverting for two-layer configurations in which the upper two layers are combined. Two-layer configurations are needed as the case of the same fabric in the two upper layers was not included in the three-layer simulations. Below 1,600 m depth, the observations of Jordan et al. (2022) are consistent with either isotropic ice or a fabric with a vertical symmetry axis. Therefore, in the lowermost layer (1,600 m depth to glacial bed at approx. 2,200 m), we predefine a vertical cone fabric of variable opening angle: one extreme of this fabric is an opening angle of 90°, equivalent to isotropic ice. In addition to these three- and two-layer configurations, we invert for "mixed"-fabric

configurations like E. C. Smith et al. (2017). The "mixed" fabric configurations are designed to compare our inversion approach to E. C. Smith et al. (2017) and always include a vertical cone and either a vertical thick girdle, a horizontal partial girdle, or a vertical partial girdle. We invert for the opening angles of these fabrics, their mixing percentage, and for the rotation of the girdle fabrics relative to North. "Mixing" of the two fabrics is calculated through Voigt-Reuss-Hill averaging (Hill, 1952; Reuss, 1929; Voigt, 1887). A detailed list of all input ice fabric configurations can be found in Table S1 in Supporting Information S1. The number of inversion parameters for the configurations considered here varies from three to seven, depending on the input configuration and the number of fabric-specific parameters inverted.

It is important to note that the parameterizable fabric distributions that we are using in this study—solid cone, girdle, and partial girdle—represent polar ice fabric in a statistical sense. Any macroscopic quantity is represented with its statistical orientation average in the seismic inversion (e.g., Maurel et al., 2015) and in the viscosity model (e.g., Gagliardini et al., 2009). Our method can only discriminate between fabrics with significantly different orientation distributions. For example, our method cannot discriminate between a solid cone, referred to as a cone in this paper, and an annular c-axis distribution, known as a cone in the microstructure community, as they could have identical orientation averages. Similarly, our method could not discriminate between a cone and a multimaxima distribution as they have similar orientation averages. However, our method can infer if ice fabric clusters in any given direction or in any given plane.

After performing inversions for all ice fabric configurations described above, we compare these outputs to find the overall best model geometry (step 3 in Figure 6). For this, three selection criteria are formulated: we aim for the parameter-set within the specific configurations that maximizes $1/\Sigma\lambda_2$' (criterion 1) and minimizes the normalized uncertainty (criterion 2). The selection based on criteria 1 and 2 is done visually by plotting a $1/\Sigma\lambda_2$' versus normalized uncertainty-graph that includes results for the best parameter-set from all ice fabric configurations. As a third criterion (criterion 3), we require that models that meet criteria 1 and 2 represent not only the first-order but also second-order features observed in the SWS results (e.g., as shown in Figure 5). As criterion 3 is less objective than criteria 1 and 2, we will introduce all models that fulfill criteria 1 and 2 in the results section and then explain their accordance to criterion 3 in the discussion section. Our ice fabric configurations feature a different number of inversion parameters. However, comparing the number of free parameters with $1/\Sigma\lambda_2$' shows no direct correlation (Figure S7 in Supporting Information S1), suggesting that much of the variations in $1/\Sigma\lambda_2$' and normalized uncertainty result from the characteristics of the input ice fabric configuration and not from the different number of free parameters.

We refrained from including more than three depth domains in the inversion. We performed tests with four-layer configurations, in which the uppermost layer was split into two 200 m thick layers. Such a geometry could be interpreted from the radar results of Jordan et al. (2022). However, the inversion algorithm could not find a stable solution for the inversion parameters in such thin layers. This was expressed by equal $1/\Sigma\lambda_2$' values for all tested values of the inversion parameters and consequentially large normalized uncertainty. This suggests that layers below 200 m thickness may be too thin to be described adequately by the inversion method used here and for the frequency content of the icequakes. By contrast, the inversion yields clear and pronounced $1/\Sigma\lambda_2$' maxima for the inversion parameters of the 400 m layer implemented in the inversion, confirming that such a layer thickness is resolvable. We also refrained from splitting the deeper layers in the inversion as the radar results do not suggest such a possibility. We also note that radar and remote sensing observations do not indicate the presence of cracks or crevasses near the surface or at the base of the ice stream in our study area, which suggests that such features do not contribute to the observed anisotropy.

4.3. Input Data for Inversion

The main advantage of the Wookey (2012) inversion method is that it operates directly on the waveforms. This has three main advantages compared to, for example, fitting a fabric model to the final SWS results. First, there is no need to introduce a quality criterion for fitting a specific fabric model as all data are fit to an underlying fabric model during the inversion. Second, null measurements, or measurements that are close to null measurements, can be included in the inversion as they contribute to the model fit with equal weight to other measurements. This is especially valuable for our data set, where initial S-wave polarization and fast direction are almost perpendicular. And third, as we apply the SWS sequentially to the waveforms for each layer, we can introduce multilayer depth configurations in the inversion.

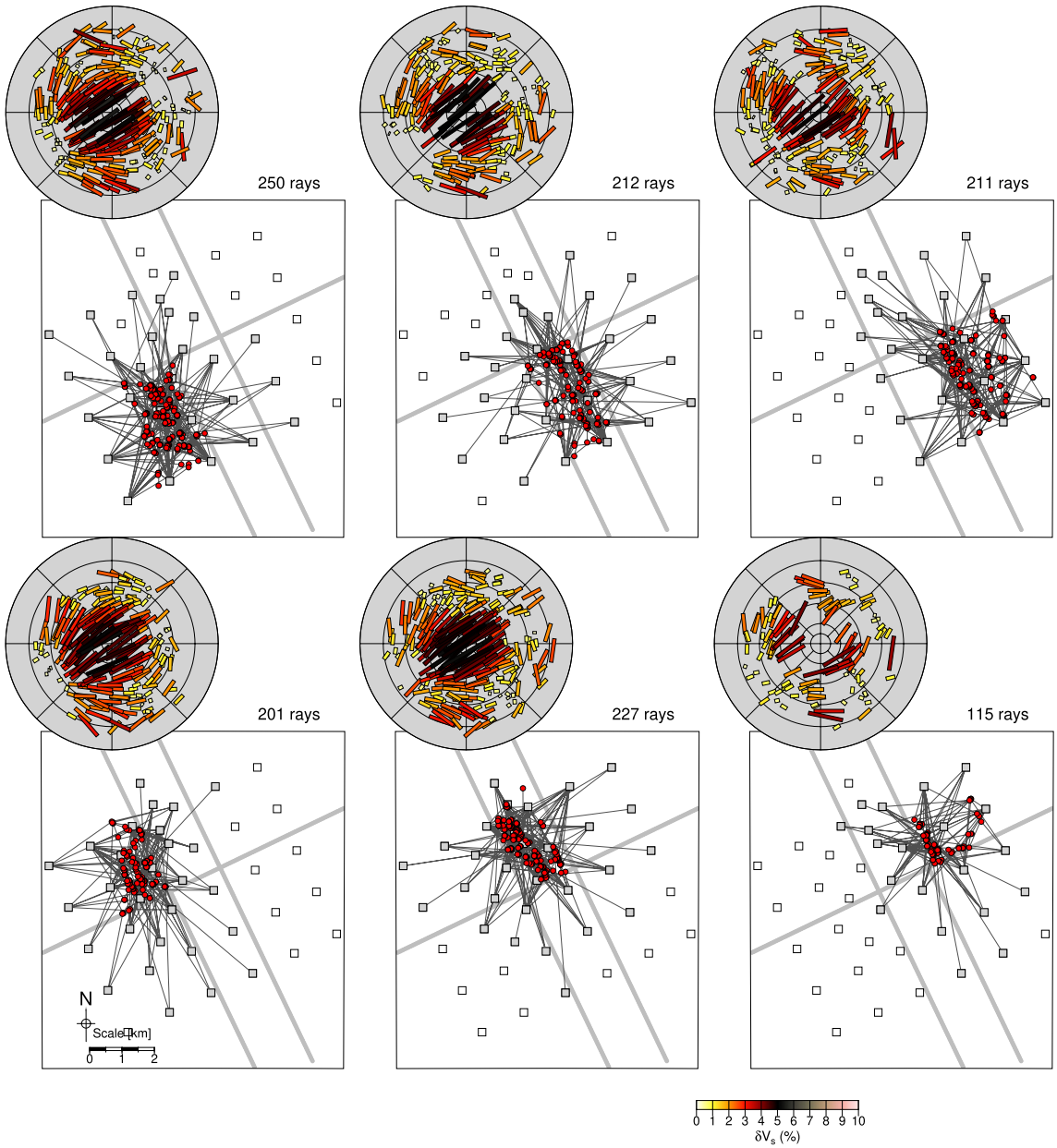

Figure 7. Input station-event pairs used for inversion on polar plots and in map view. To ensure an equal distribution of rays throughout the study region, we separate the study region into six domains. Input rays of these domains are highlighted in the six subplots. The separation between the domains is arranged parallel and perpendicular to the ice flow direction (marked by light gray lines). Polar plots show splitting measurements color coded by δV_S and are in the same nomenclature and coordinate system as used in Figure 4. The maps are in the same projection as Figure 2 and highlight station-event pairs (gray squares & red circles respectively) used in the inversion. The total number of rays (thin gray lines) used from a specific domain is given in the top-right of each plot.

The drawback of the method is that each input waveform contributes equally to the final solution. Therefore, an equal distribution of input data throughout the entire range of incidence angles and azimuths is important. To satisfy this requirement, we use only a representative subset of all waveforms for which we have calculated SWS results as input for the inversion. To ensure a representative distribution of rays throughout the study region, we separate the region into six lateral spatial domains, with the boundaries arranged parallel and perpendicular to the ice flow direction (Figure 7). For each of these domains, we choose a subset of available waveforms based on the averaged SWS results (Figure 5). The selection of the subset was driven by two main factors: we aimed for both high-quality data and for an equal distribution of input data with respect to incidence angle and azimuth. Thus, for each spatial domain and for each of the averaged incidence angle-azimuth bins, only the best station-event pair is chosen: "best" refers

to the event-station pair with the largest cross-correlation coefficient of the corrected and rotated waveforms and the smallest uncertainty in Φ and δV_S. In addition, only events for which the cross-correlation coefficient is larger than 0.5 and the uncertainty in Φ and dt is smaller than 10° and 0.001 s, respectively, are included. Lastly, only events from incidence angle-azimuth bins for which the standard deviations of Φ and δV_S are smaller than 30° and 1.2% are included. These criteria ensure that the event-station pairs used for inversion are representative of the entire data set. The final data set then consists of 1,216 event-station pairs (Figure 2a; also shown in Figure 7 in more detail). We performed a test of this step: using fewer measurements yielded biased results due to an unequal event distribution in terms of azimuth and incidence angles; using more results drastically increased computation time whilst not improving the results, as it became increasingly difficult for the inversion algorithm to find a stable global maximum.

4.4. Inversion Results and Selection of Best Models

To qualitatively compare the best parameter-sets from all ice fabric configurations, we plot $1/\Sigma\lambda_2$' versus normalized uncertainty (Figure 8 and Figure S8 in Supporting Information S1). Figure 8 illustrates that all results plot in a broad band of scattered normalized uncertainty that describes a roughly linear trend from small to large $1/\Sigma\lambda_2$' values. Neither two-layer configurations nor three-layer configurations that feature a cone fabric in the thickest layer can explain SWS to a satisfying degree. The two-layer configurations allow too little flexibility to capture finer scale trends in the data. A cone fabric, even when oriented horizontally, cannot account for the large δV_S at small incidence angles. In Figure 8, we highlight the four configurations for which the best parameter-sets demonstrate a combination of large $1/\Sigma\lambda_2$' and small normalized uncertainty and are therefore most compatible with our measurements. Thus, these four models fulfill the selection criteria 1 and 2 as specified in Section 4.2. We refer to these as Models A-D in the following. Details of these models are given in Figures 9–11 and Table S2 in Supporting Information S1.

Interestingly, these four most suitable models are composed of different fabrics (Figure 9). One is a 'mixed' model (Figure 9a) composed of a vertical cone and a horizontal partial girdle. The other three are three-layer models consisting of (a) a vertical partial girdle in the center and a horizontal partial girdle in the top layer (Figure 9b), (b) a horizontal partial girdle in the center and a horizontal cone in the top layer (Figure 9c), and (c) a vertical thick girdle in the center and a tilted cone in the top layer (Figure 9d). The uncertainties in the fabric parameters vary for the different models (Figure 10; Table S2 in Supporting Information S1). When looking at the uncertainties of the individual parameters, the azimuthal orientation of the fabric in the middle layer (domain 2 in Figure 9) is constrained best, while the opening angle of the vertical cone in the bottom domain (domain 1) has a higher uncertainty. However, in a more general sense, the uppermost layer is the most difficult to constrain, demonstrated by its fabric type varying between the different models.

Figure 11 shows two further ways to present the inversion results. On a polar plot, either the λ_2' pattern for the individual rays or the resulting δV_S and Φ can be plotted. In this representation, inversion results can be directly compared to SWS results (e.g., Figure 4 or Figure 5). While SWS results are derived from minimizing λ_2' for each ray individually, the inversion results are based on the specific ice fabric configuration and the maximization of $1/\Sigma\lambda_2$' for all rays. Calculating the δV_S and Φ parameters for each event individually best minimizes λ_2'. The sum of all λ_2' is 0.32 (obtained by summing up λ_2' values from all rays) in the case of the input data used in inversion. This small value arises as we chose the highest quality subset from all SWS results, which is characterized by small λ_2' values (Figure 11a). For the best inversion model, the sum of all λ_2' is 2.71, which corresponds to a reduction of 23% relative to the uncorrected data ($\Sigma\lambda_2' = 3.53$).

Despite being composed of different fabric elements, all four best models (Models A-D) obtained from the inversion have similarities with the main features described in Section 3.2. These are a higher percentage of anisotropy for small incidence angles and an alternating pattern of smaller and larger δV_S for larger incidence angles (Features f1/1x, f2, and f3/3x in Figure 4). However, only the fourth model (Model D) can explain the asymmetry of the SWS data relative to the ice flow direction (features f4/f4x and f1x, f2x in Figure 4). The recovery of these secondary features was another constraint we put onto the inversion results (see workflow in Figure 6). In the case of Model D, the recovery of secondary features arises from the tilted cone fabric in the uppermost domain of the model (domain 3 in Figure 9d).

5. Discussion and Interpretation

5.1. Unambiguously Constrained Fabric Components

Generally, we found that the greater the layer thickness the greater its impact on the inversion result. Therefore, we observe more consistent results in the lower two layers (thicker) and more variation in the uppermost layer

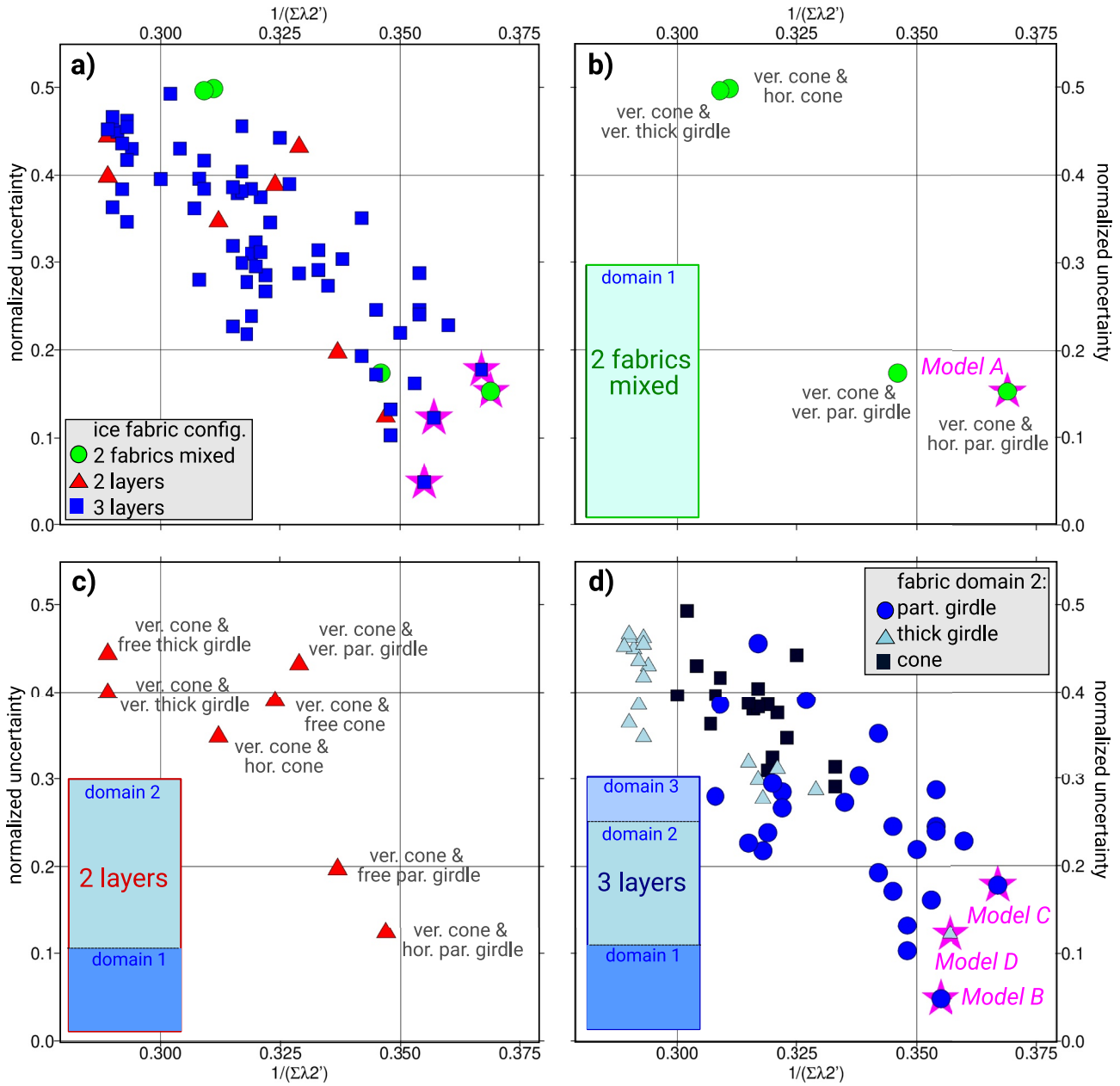

Figure 8. Comparison of inversion results for different input ice fabric configurations. For all configurations, only one parameter-set, the one that features the largest $1/\Sigma\lambda_2'$, is plotted. (a) All specified configurations are plotted (see details in Table S1 in Supporting Information S1). The overall best models (Models A-D in Figures 9–12), which meet selection criteria 1 and 2 (see Section 4.2 for explanation), feature large $1/\Sigma\lambda_2'$ and a small normalized uncertainty are highlighted in purple. Plot colors and symbols refer to the input geometries. (b) Annotated plot showing only mixed ice fabric configurations. Inset schematically shows the ice fabric configuration. (c) Annotated plot showing only two layer-configurations. (d) Only three-layer configurations are shown. Color and symbols represent the fabric of the central layer. See Figure S8 in Supporting Information S1 for a plot where all configurations are annotated in more detail.

(thinner) of the three-layer models B-D. While the lowermost layers contribute to the first order characteristics of the SWS pattern, the uppermost layer mostly adds secondary features. Thus, although composed of different fabric types, the four models A-D with statistically comparable fits (Figure 9) share several similarities: First, the vertical cone, which was predefined in the lowermost ice fabric layer, or as one fabric component of the "mixed" configuration, has a wide opening angle (>70°) in all four models A-D. Second, the fabrics in the middle and top layers, or the second fabric component in the "mixed" model, are oriented approximately perpendicular to the ice flow direction. Lastly, the fabric in the middle layer, or the second component in the "mixed" model, produces the largest δV_S in a band perpendicular to ice flow. It is due to the characteristics of the observed SWS pattern

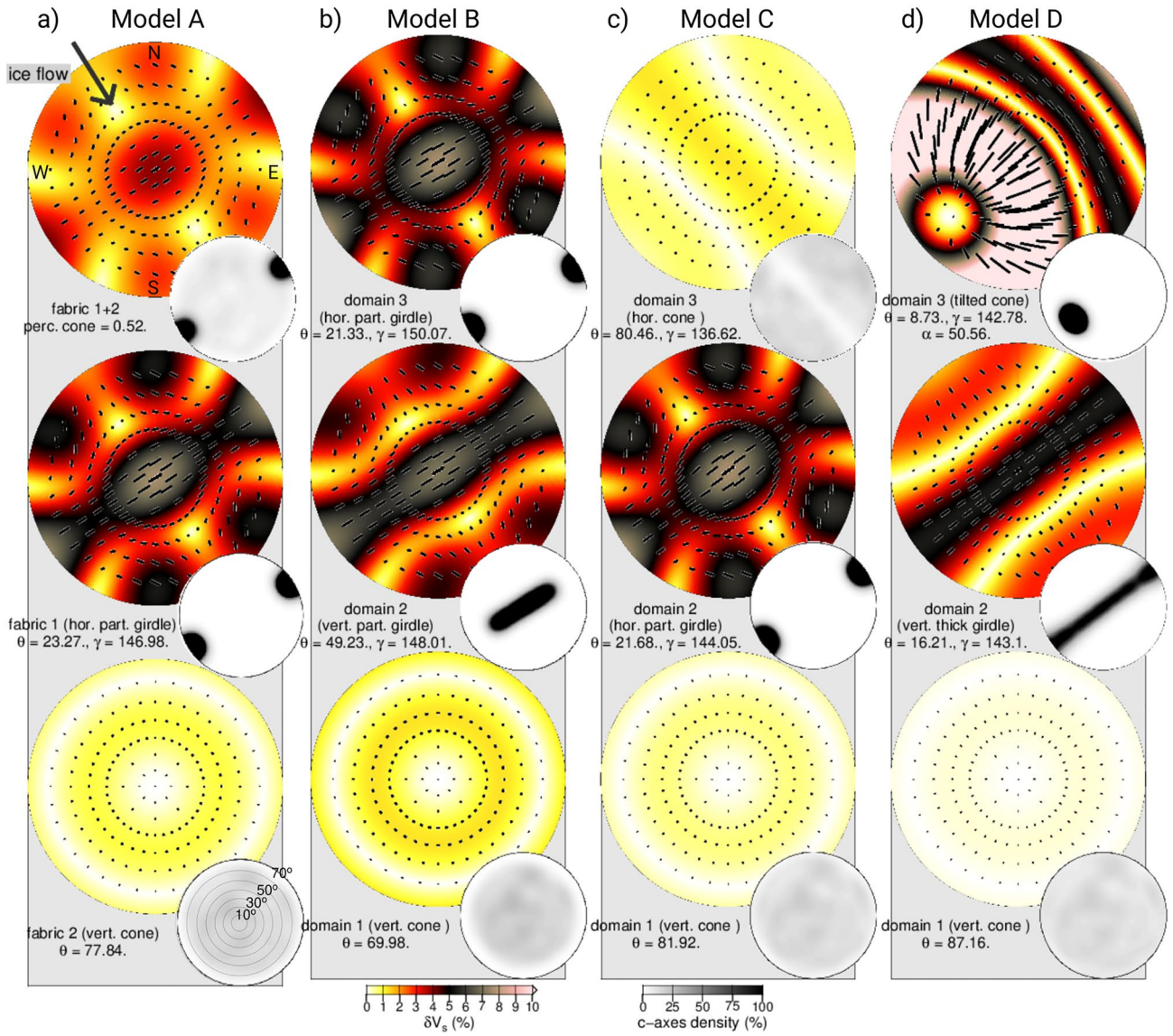

Figure 9. Inversion results for each depth domain and fabric type from the four best models as upper hemisphere plots. Note that the scale of the plotted incidence angles changed compared to Figures 4 and 5 (see inset in the bottom left for the new scale). The associated coordinate system is plotted in Figure 1. Ice flow direction of Rutford Ice Stream is highlighted with a black arrow. Note that the incidence angles here refer to those of the rays in ice, which are less steep than those at the surface due to the velocity gradient in the firn. This convention is chosen when visualizing the inversion results as the majority of the ray paths is through the ice layer. Insets show associated c-axes distribution in grayscale. (a) Results from "mixed" fabric inversion. The top panel shows the shear-wave splitting pattern obtained from combining the two fabrics, using Voigt-Reuss-Hill averaging. (b–d) Results from three-layer inversion. Each polar plot represents results from one depth layer. See Table S2 in Supporting Information S1 and Figure 10 for the uncertainty ranges of the parameters. As argued in Section 5.2, we consider Model D as the most likely.

(Figures 4 and 5) and due to the anisotropy characteristics of the different ice fabrics, that multiple combinations are numerically comparable. Nevertheless, the inversion revealed that a basal broad cone fabric in combination with a fabric which features the elements described above, is essential to explain the SWS pattern of RIS.

In addition, the inversion unambiguously allows us to exclude several scenarios. First, it is unlikely that a horizontal cone fabric exists in the central layer. Such a fabric features anisotropy perpendicular to flow and at small incidence angles that is too low and therefore not compatible with the SWS measurements. This is an important additional contribution to the interpretation of results from radar surveys, as those data cannot discriminate between a horizontal cone or a vertical girdle fabric. Lastly, we performed a sensitivity analysis (Section S3 and Figure S9 in Supporting Information S1), where we tested the impact of the vertical cone fabric and the impact of the predefined layer depth on the final solution. These tests showed that placing a vertical cone fabric in the

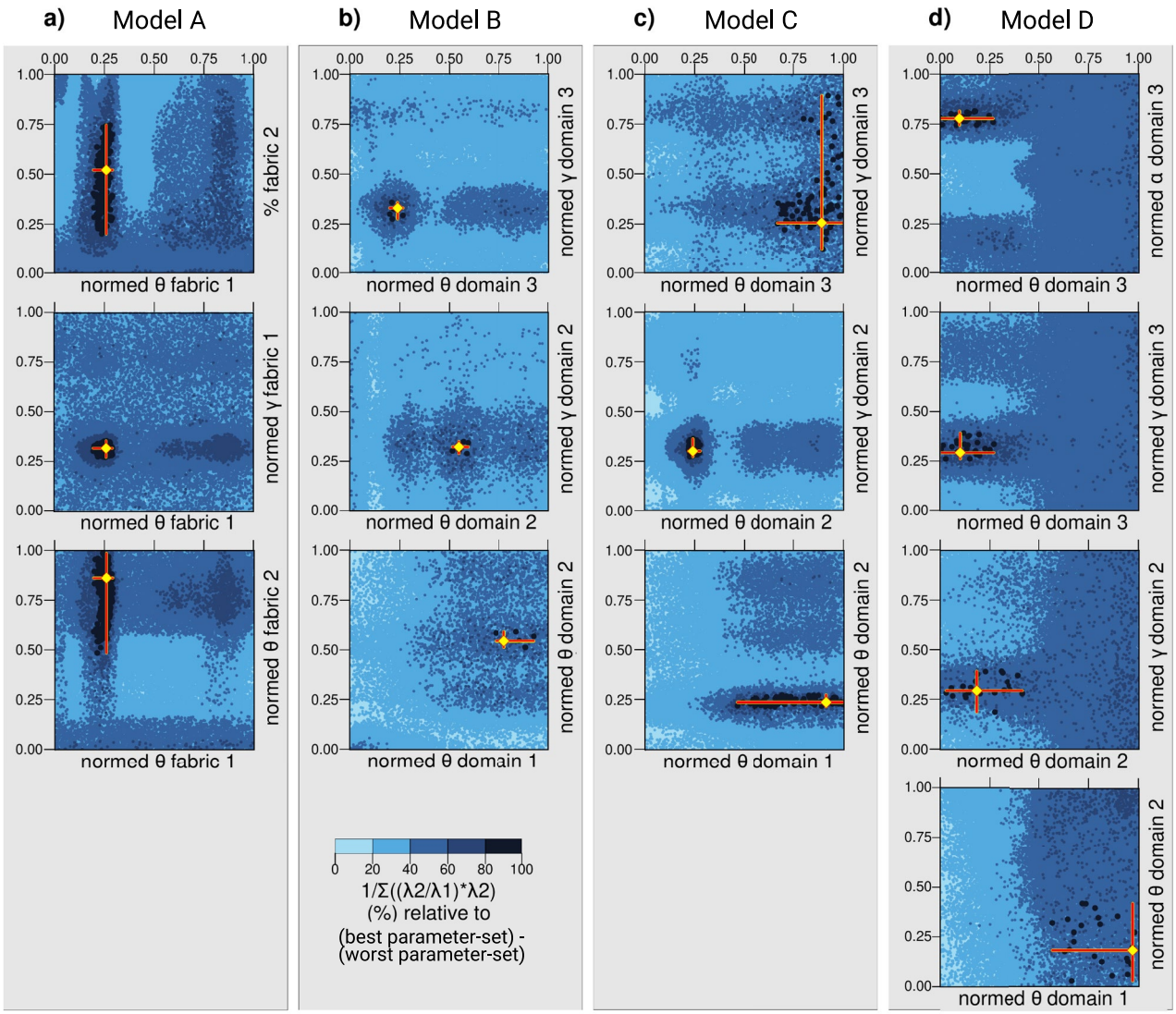

Figure 10. Uncertainty of the ice-fabric parameters for the four models presented in Figure 9. All parameters are normalized to the range from 0 to 1. See Table S2 in Supporting Information S1 for the values in degrees and Figure 1 for the coordinate system used. (a) "Mixed" model as presented in Figure 9a. Fabric 1 is a horizontal partial girdle, fabric 2 a cone. (b–d) 3-layer models as presented in Figures 9b–9d.

central layer, or excluding the vertical cone from the inversion, decreased $1/\Sigma\lambda_2$'. Thus, the sensitivity analysis emphasizes that a vertical cone fabric at the base of RIS is an essential element, independent of which of the models A-D is chosen. In addition, the sensitivity analysis showed that the input geometry initially defined yielded the best results (parameter-sets with largest $1/\Sigma\lambda_2$' for specific ice fabric configurations). This illustrates that using radar results to define the input ice fabric configuration is a valid and important tool when inverting SWS data for ice fabric.

5.2. Three-Layer Model With Vertical Thick Girdle Fabric in Central Layer (Model D) as the Preferred Solution

Despite the fact that there are several different models with statistically comparable fits, we favor the fourth model (Model D; Figure 9d) as it is the only one that can additionally explain the fine-scale trends, or second-order features, observed in the SWS results (Figures 4 and 5), which was an additional constraint we put onto our final inversion results (criterion 3 in Section 4.2 and step 3 in Figure 6). Model D features three depth layers with a thick vertical girdle fabric in its middle layer.

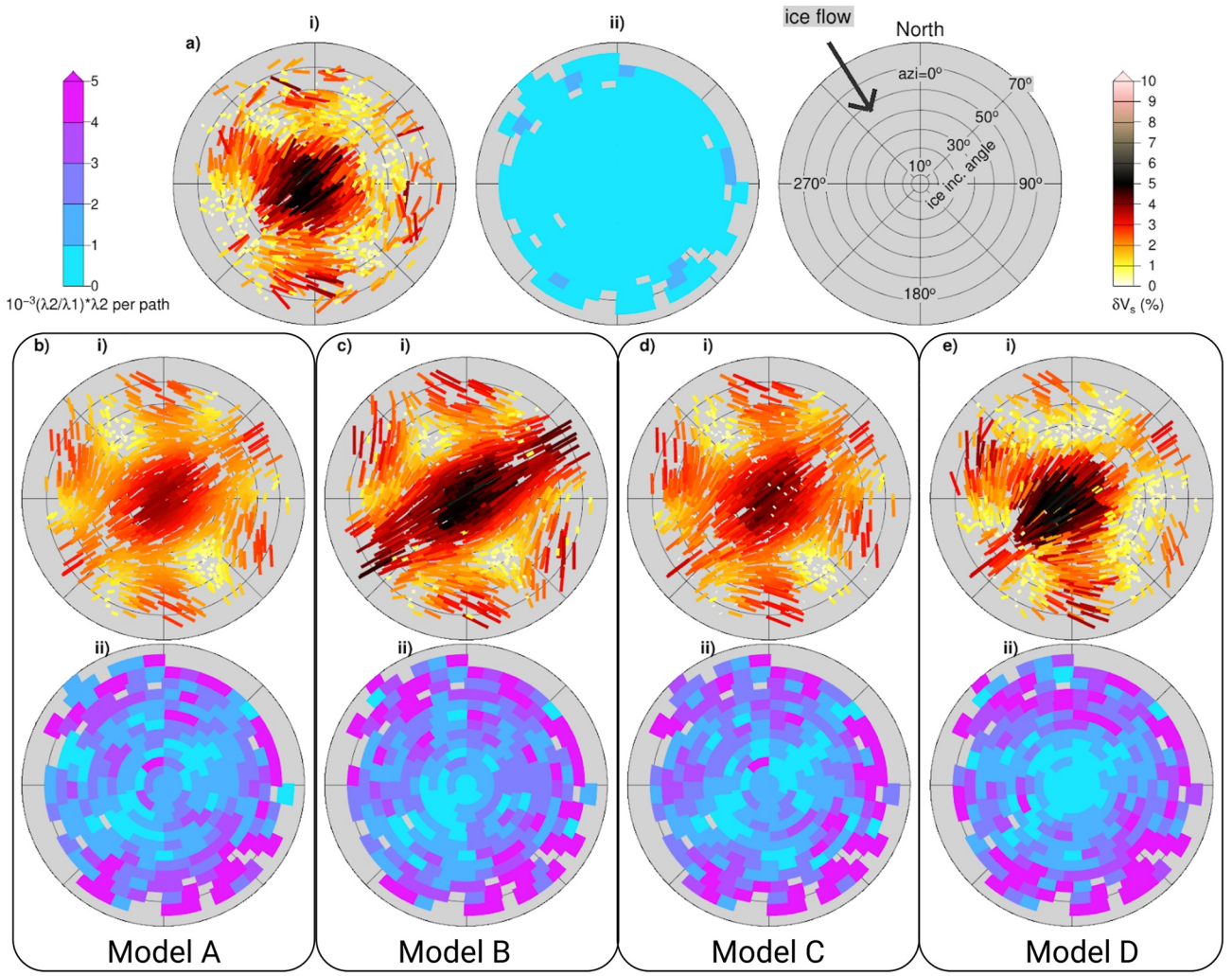

Figure 11. Inversion results from the four best models compared to shear-wave splitting (SWS) results. Subfigures i show an upper hemisphere plot of SWS parameters for each ray (azi = 0° corresponds to North; ice flow direction at Rutford Ice Stream is highlighted with a black arrow), while subfigures ii show λ_2', averaged in bins, similar to Figure 5. We here use λ_2' instead of $1/\lambda_2$' to allow a direct comparison to the SWS results, where λ_2' = 0 would correspond to the complete removal of SWS splitting and thus the best possible result. Note that the way how the ray incidence angle is plotted changed compared to Figures 4 and 5. Instead of the incidence angle expected at the surface, the incidence angle of a ray through the ice is plotted. As the ray paths are mostly through the ice, this representation is more suitable when comparing the results to the ice-fabrics plotted in Figure 9. (a) SWS parameters and λ_2' from SWS-analysis for each ray individually. In contrast to for example, Figure 4, where all results are shown, we here plot only the high-quality subset, which had been used as input for inversion ($\Sigma\lambda_2$' = 0.32). (b–e) SWS parameters and λ_2' from inversion for ice fabric. (b) Results from the inversion for a combination of a vertical cone and a horizontal partial girdle ($\Sigma\lambda_2$' = 2.72). (c) Results from a three-layer inversion with a vertical cone at the base, a vertical partial girdle in the center and a horizontal partial girdle in the top layer ($\Sigma\lambda_2$' = 2.81). (d) Results from a three-layer inversion with a vertical cone at the base, a horizontal partial girdle in the center and a horizontal cone in the top layer ($\Sigma\lambda_2$' = 2.74). (e) Results from a three-layer inversion with a vertical cone at the base, a vertical thick girdle in the center and a tilted cone in the top layer ($\Sigma\lambda_2$' = 2.80).

One of the three thus excluded models is a "mixed" fabric model (Figure 9a) for which no layering is assigned. Instead, a uniform ice fabric consisting of two fabric types combined throughout the entire ice column was assumed. The parameters we derive for this model are consistent with the preferred solution of E. C. Smith et al. (2017) within the measurement uncertainties (Θ cone = 73°; Θ hor. partial girdle = 22°; γ = 144°; mixing percentage = 53% vs. here: Θ cone = 78°; Θ hor. partial girdle = 23°; γ = 147°; mixing percentage = 52%). This consistency validates the inversion approach chosen here. However, in addition to the fact that it does not explain the fine scale structure in our data, several other arguments suggest that the "mixed" model is unlikely to represent the true ice fabric of RIS. First, the "mixed" model is hard to explain physically. A distinct deformation regime results in a specific ice fabric. Therefore, and as also noted by E. C. Smith et al. (2017), the "mixed" model rather suggests that the two fabric types exist within the ice but with their depth distribution unresolved. Second, radar imaging (Jordan et al., 2022) clearly shows that layers of distinct ice fabric exist at RIS, which is incompatible with a

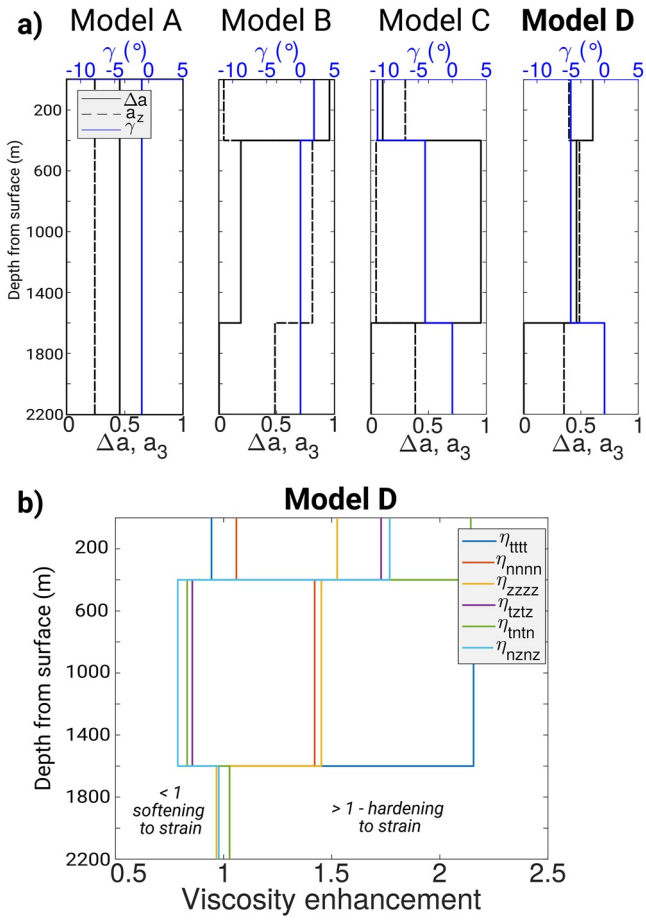

Figure 12. (a) Fabric orientation tensor for the four models shown in Figures 9–11. Tensors are represented as differences between the horizontal eigenvalues (Δa), the horizontal azimuth with respect to the flow direction (γ), and the vertical eigenvalue (a_z). Δa and γ can be measured from downward-looking radar, whereas a_z cannot be measured. Model labels as in Figure 9. (b) Principal components of the viscosity enhancement tensor for Model D (Figure 9d), highlighting that viscosity strongly depends on the component of deformation. Consistent with Jordan et al. (2022), we use a natural flow frame of reference: t represents tangential to flow, n normal to flow and z is the vertical.

uniform ice fabric. Lastly, the few available ice cores from areas of flowing ice (although not Antarctic Ice Streams) do observe rather thick girdle fabrics (Jordan et al., 2020; Stoll et al., 2018), potentially suggesting that the partial girdle is less prevalent. Combining these arguments, we prefer to rule out the "mixed" model as a likely candidate. The reason this model yields results comparable to the three-layer models B-C is a result of the specific fabric combination, with the broad cone modifying the waveforms little. For example, if the cone fabric would have a smaller opening angle, corresponding to more anisotropic ice, a "mixed" model and a two-layer model, with a layer thickness comparable to the mixing percentage, would yield different results.

The two other three-layer models B and C, which feature a horizontal or vertical partial girdle fabric in the central layer (Figures 9b and 9c) also seem unrealistic. Although these models are compatible with results from radar, they also feature an ice fabric type as the main contribution that has not been observed elsewhere. In addition, and possibly more importantly with regards to our selection criteria (step 3 in Figure 6), these models do not reproduce the distinct asymmetry relative to ice flow, observed from the SWS data (features f1/f3/f4 vs. f1x/f3x/f4x in Figure 4) and also overestimate the flow-perpendicular anisotropy at incidence angles greater than 30° degrees (features f4/f4x in Figure 4).

Only Model D (Figure 9d) is both compatible with the radar results and captures the secondary features of the SWS results. In addition, Model D is composed of fabric elements that are commonly observed in ice cores and captures the asymmetry in the SWS data relative to the ice flow direction. The asymmetry is due to the tilted cone fabric in the uppermost layer. Potentially, the flow-perpendicular asymmetry in the SWS data set could be caused by spatially variable fabric beneath our network. However, we consider this scenario as unlikely as we did not find a clear signal of spatially variable fabric in the SWS data (see Text S1 in Supporting Information S1). In addition, the SWS patterns from the different spatial domains, which we used to generate the input for inversion, also reveal the asymmetry (Figure 7). These different elements lead us to conclude that the Model D represents the most likely fabric configuration at RIS.

As only Model D (Figure 9d) captures the flow-perpendicular asymmetry in the data, one might argue that $1/\Sigma\lambda_2$' is not the ideal measure to characterize the quality of the inversion results. We experimented with using $1/\Sigma\lambda_2$ instead but found that this destabilized the inversion in a way that makes it more difficult for the algorithm to find a global maximum. We further refrained from using any weighting function, for example, weighting input data with smaller split times differently, as this would introduce a bias in the input data. The input waveforms were chosen based on distinct quality criteria and an equal distribution of the input data with regards to azimuth and incidence angle was guaranteed. Thus, this analysis shows that it is due to the specific geometry of the anisotropy pattern that the results from one "mixed" and three three-layer models appear equally good. However, as argued above, we are confident that the inversion, together with additional information from other studies, allows us to assign Model D (Figure 9d) as the most likely.

5.3. Impact of Preferred Solution (Model D) on Mechanical Properties

To demonstrate the impact of the measured fabric on ice flow, we estimate the resultant viscosity tensors, an important parameter in flow-laws for ice sheet models. We follow the method of Jordan et al. (2022) where the c-axis orientation distribution is represented with a second-order orientation tensor. The eigenvalues of this tensor represent the relative c-axis concentration along the principal coordinates. Jordan et al. (2022) highlight how the lack of information on the vertical component of the fabric in downward-looking radar observations

($0 < a_z < 1 - \Delta a$) translates into a large uncertainty in ice properties for fast-flowing ice. Unlike these methods, which are limited to measuring the orientation of the horizontal eigenvectors and their relative strength, the results from the SWS inversion allow us to estimate the amplitude and orientation of all three eigenvectors in the principal axes. We follow the scheme of Jordan et al. (2022) to derive the viscosity enhancement due to fabric to understand the effects of the measured fabric on viscosity and deformation.

Figure 12a presents the eigenvalue representation of the four best fit models A-D described above. To allow direct comparison with existing downward-looking radar observations, we represent the orientation tensor in natural flow coordinates, where t represents the horizontal direction of ice flow, n is normal to flow in the horizontal and z is the vertical. Under the assumption that the vertical is a principal vector, the orientation tensor can be represented by the difference in horizontal eigenvalues (Δa), azimuth of the fabric with respect to the direction of flow (γ) and the vertical component of the orientation tensor (a_z) (Jordan et al., 2022). This representation clearly emphasizes the differences between the four models with respect to ice viscosity despite the similarity in SWS patterns.

Ice viscosity is often divided into an isotropic component, related to the ice flow-law, and an anisotropic component, related to the ice fabric (Ma et al., 2010; Martín et al., 2009). We use GOLF anisotropic flow-law (Gillet-Chaulet, 2006) from the ElmerIce AIFlow solver (Gagliardini et al., 2013) to calculate the latter. The solver searches viscosity for a given second-order orientation tensor in a space that has been tabulated using different viscosity models and crystal-scale parameters. Following Jordan et al. (2022), we assume that $\beta = 0.04$, the ratio of viscosity of the grain for shear parallel to the basal plane to that in the basal plane; $\gamma = 1$, the ratio of the viscosity in compression or tension along the c-axis to that in the basal plane; and the model used for tabulation is a viscoplastic self-consistent model (Castelnau et al., 1996).

Figure 12b then presents the derived viscosity enhancement factors due to fabric for the most representative components for our preferred model (Model D). Values greater than one represent stiffening or hardening to strain and values lower than one softening. In the shallowest layer, we see a complex range of softening and hardening, with the most significant effects on η_{nznz} (hardening to vertical shear perpendicular to flow), η_{tntn} (hardening to lateral shear), and η_{tztz} (hardening to vertical shear parallel to flow). However, the bulk of the ice column, in the middle layer, exhibits hardening to compression or extension along flow with an enhancement factor of $\eta_{\mathrm{tttt}} = 2.16$, which equates to a factor of 10 in viscosity due to the third power if, as commonly assumed, we use 3 for the rheological index in Glen's flow-law (Ma et al., 2010; Martín et al., 2009). Also, in the middle layer, ice is 3.5 times softer to compression or extension across flow than along flow [$(\eta_{\mathrm{tttt}}/\eta_{\mathrm{nnnn}})^3 = 3.5$] and 16 times softer to shearing than to compression or extension along flow [$(\eta_{\mathrm{ttt}}t/\eta_{\mathrm{tztz}})^3 = 16$]. We see little effect in the deepest layer of the ice column. This shows that the character of ice deformation not only depends on the direction of applied force but also on the depth within the ice column.

5.4. Formation Scenario for Preferred Ice Fabric (Model D)

Ice fabric at a specific location is a combination of the strain history and recrystallization processes (Alley, 1988). Ice fabric is not instantaneously developed and our results thus point to a complex strain history of RIS. Here, we discuss potential formation mechanisms for an ice fabric as resolved in Model D (Figure 9d). For this interpretation, it is important to consider that the parameterizable fabric distributions that we are using in this study only represent polar ice in a statistical sense. For example, the method does not allow us to discriminate between a solid cone and an annular c-axis distribution. However, the direction and plane in which ice fabric clusters can be inferred.

In the upper 400 m layer, a tilted cone fabric is inferred. Such a fabric could arise through a combination of horizontal shearing across flow and compression. We suggest that this fabric represents the cumulative effect of complexity in the shallow ice column that is "averaged" using the SWS method. An ice layer, which is characterized by intense deformation and rotated layers, seems plausible based on other available datasets: Radar measurements show a complex finer scale depth structure near the surface of RIS (Jordan et al., 2022) and fabric is known to develop quickly in areas of fast-flowing ice (Montagnat et al., 2020). Given that snow accumulation rates at RIS at our study site are about 0.5 m/yr (after Doake et al., 1987), the ice to 400 m depth has been deformed for a period of several hundred years. We can exclude effects like crevassing for our study site as contributing to the anisotropy in the upper layer as no crevasses are present (Jordan et al., 2022).

In the middle layer the inferred fabric is dominated by a thick vertical girdle, oriented perpendicular to flow. Such a fabric can be formed due to extension along flow. Such a deformation regime is consistent with the surface strain measured ∼30 km upstream of our study region, which is dominated by along-flow extension at the surface (Jordan et al., 2022), and would result in this fabric geometry. Considering the above-mentioned snow accumulation rates at RIS, the study site of Jordan et al. (2022) is too close to our study region to explain the observed fabric below 400 m depth. Nevertheless, the Jordan et al. (2022) study showed that the surface flow regime of Rutford can change over small distances. It is therefore feasible that the fabric measured here in the middle layer was formed by extensional flow upstream of the current location, and subsequently buried and advected to the experiment site.

Our results suggest that a vertical cone fabric with a wide opening angle, almost an isotropic fabric, dominates the deepest layer. At this depth, there are two possible formation mechanisms for a vertical cone fabric. A vertical cone can develop where basal shear dominates over basal sliding. In the extreme scenario, where ice is stagnant, the main component of strain will be vertical compaction, again resulting in a vertical cone fabric. Alternatively, the fabric may form by ice migration recrystallization, that tends to replace an existing population of grains with a new population of grains and making it less dependent on flow-induced development (Alley, 1992). At RIS, large numbers of icequakes are observed at the ice-bed interface (Kufner et al., 2021; E. C. Smith et al., 2015), indicating that basal sliding dominates over basal shear, and it is likely that a similar regime existed in the past (Gudmundsson & Jenkins, 2009). Ice recrystallization is therefore a more likely fabric formation process than basal shear dominating over sliding. We note however, that the uncertainties on the opening angle of the basal cone are large (e.g., up to −36° for our preferred model) and asymmetrically distributed (i.e., the uncertainty toward smaller opening angles is larger). Nevertheless, even opening angles larger than for example, 40° are more than is observed in ice-cores from ice divides (e.g., Pettit et al., 2007). At RIS, the recrystallization and thus formation of new ice crystals might also explain the wide opening angle of the observed cone fabric.

Interestingly, the ice fabric we infer for the bottom part of RIS is very similar to that observed for the entire ice column below the firn at Whillans Ice Stream using active seismic imaging (Picotti et al., 2015). They suggested that ice fabric formation is dominated by vertical compression rather than internal extensional deformation. However, Picotti et al. (2015) note that the ice fabric further upstream might be a vertical girdle, which is erased at their study side. In contrast to Whillans Ice Stream, our analysis at RIS shows the basal cone layer to be overlain by an ice layer with a different fabric that testifies to predominantly along-flow extension. Potentially, multiple layers of different ice fabrics could evolve at RIS due to its larger ice mass (RIS is much thicker than Whillans Ice Stream; ∼780 vs. ∼2,200 m at RIS). Alternatively, these observations might emphasize that the ice fabric along the length of an ice stream is highly variable due to both strain history and recrystallization. This would imply that multiple fabric studies along the length of an ice stream are needed to understand its current deformation. Lastly, it should be noted that our method resolves only large-scale characteristics (i.e., >200 m thickness; see Section 4.2) of the ice in the anisotropy-intensity range considered here. This is mainly due to the uncertainty in the SWS measurements. Therefore, we cannot rule out a thin layer of ice (e.g., several meters) at the base of RIS with a fabric different from the vertical cone. Similarly, the uppermost layer discussed here includes the firn (upper ∼100 m), which is likely less anisotropic than the ice below it (E. C. Smith et al., 2017).

6. Summary and Conclusions

We present more than 200,000 SWS measurements from RIS, a fast-flowing (>1 m/day), ∼2.2 km thick West Antarctic ice stream. Results indicate seismic anisotropy of up to 6.6% in the glacial ice. The degree of S-wave anisotropy varies, however, depending on azimuth and incidence angle of the seismic ray paths. These variations are much stronger than temporal or spatial variations in the SWS pattern.

We invert the data for depth-dependent ice fabric, making use of the fact that different types of fabrics can be discriminated from each other based on their anisotropic pattern. Ice fabric is represented in a statistical sense (e.g., Maurel et al., 2015). The structure of the input ice fabric configurations for inversion is designed based on prior information from radar studies (Jordan et al., 2022). The inversion shows that the SWS pattern is statistically equally well explained by four different models (models A-D in Figures 8–12). One of the models (Model A) is a combination of a vertical cone fabric and a horizontal partial girdle fabric. The other models B-D feature three layers of different ice fabrics for the middle and top layers. In all four models, the deepest layer (500 m thickness) is a vertical cone fabric. For all four models, inversion yields a large (>70°) opening angle for this

lowermost layer. One such model (Model B) consists of a vertical partial girdle in the middle layer (1,200 m thickness) and a horizontal girdle in the uppermost layer (400 m thickness). The next model (Model C) features a horizontal partial girdle (middle) and a horizontal cone (top). The last model (Model D) features a vertical girdle (middle) and a tilted cone (top). As only the last model (Model D in Figure 9) reproduces a distinct asymmetry of the seismic anisotropy relative to ice flow, which can be seen in the SWS results, we favor this model as the most realistic. In addition, the central vertical girdle agrees with ice core results obtained in areas of flowing ice (Jordan et al., 2020; Stoll et al., 2018).

A fabric as resolved in the deepest layer of Model D could arise from mostly vertical compression due to high basal shear at the base of the ice stream. The shearing itself may add to the creation of the cone fabric as well. Alternatively or in addition, recrystallization of the ice in the basal unit may yield a broad cone fabric. The middle and upper layers could arise mostly from extension along flow at central depths and a mixture of horizontal shear across flow and compression near the surface. We suggest that such a scenario might have formed from a combination of past and current deformation under different stress regimes, likely in combination with ice recrystallization.

We calculate the viscosity enhancement factor for the preferred ice fabric model (Model D) and find that the middle layer is significantly (3.5 times) harder to deform along flow than across flow. By contrast, there is little directional effect in the deepest layer. Thus, a single enhancement factor for the entire depth range of the ice column, as often used in ice sheet models, is unlikely to represent the viscosities determined here. It remains a topic of future research if SWS splitting at RIS is representative for fast-flowing ice streams in general or if the observed pattern is predominantly controlled by local factors.

This study shows that passive seismic imaging can help to constrain ice fabric at far lower cost than through direct measurements (e.g., boreholes) if prior knowledge of the depth structure of the ice is available. Furthermore, results from SWS complement other passive geophysical methods such as radar imaging, as the ice fabric in all three dimensions can be constrained.

Data Availability Statement

Data: Waveform data and SWS results (Kufner et al., 2022) can be accessed via the Polar Data Center. The data set can be accessed directly via this URL: https://ramadda.data.bas.ac.uk/repository/entry/show?entryid=6fc-c17ad-425b-4367-bd23-c4133a38e359. *Software*: Version 2.2 of MFAST used for SWS analysis is available via https://mfast-package.geo.vuw.ac.nz/. The software used for ice fabric inversion is still under development and the authors of this manuscript can be contacted via mail for requests.

Acknowledgments
This work was funded by NERC AFI award numbers NE/G014159/1 and NE/G013187/1. The authors thank the staff at Rothera Research Station and BAS Logistics for enabling the fieldwork associated with this project and the BEAMISH field team (2018/2019) for acquiring the passive seismic data. Seismic instruments were provided by NERC GEF (Loan 1017), BAS, and the Incorporated Research Institutions for Seismology (IRIS) through the PASSCAL Instrument Center at New Mexico Tech. The facilities of the IRIS Consortium are supported by the National Science Foundation's Seismological Facilities for the Advancement of Geoscience (SAGE) Award under Cooperative Support Agreement EAR-1851048. We thank three anonymous reviewers and the editors for thoughtful comments that significantly improved this manuscript.

References

Adalgeirsdóttir, G., Smith, A. M., Murray, T., King, M. A., Makinson, K., Nicholls, K. W., & Behar, A. E. (2008). Tidal influence on Rutford ice stream, West Antarctica: Observations of surface flow and basal processes from closely spaced GPS and passive seismic stations. *Journal of Glaciology*, *54*(187), 715–724. https://doi.org/10.3189/002214308786570872

Alley, R. B. (1988). Fabrics in polar ice sheets: Development and prediction. *Science*, *240*(4851), 493–495. https://doi.org/10.1126/science.240.4851.493

Alley, R. B. (1992). Flow-law hypotheses for ice-sheet modeling. *Journal of Glaciology*, *38*(129), 45–256. https://doi.org/10.1017/S0022143000003658

Azuma, N., & Goto-Azuma, K. (1996). An anisotropic flow law for ice-sheet ice and its implications. *Annals of Glaciology*, *23*, 202–208. https://doi.org/10.3189/s0260305500013458

Budd, W. F., Warner, R. C., Jacka, T. H., Li, J., & Treverrow, A. (2013). Ice flow relations for stress and strain-rate components from combined shear and compression laboratory experiments. *Journal of Glaciology*, *59*(214), 374–392. https://doi.org/10.3189/2013JoG12J106

Castelnau, O., Duval, P., Lebensohn, R. A., & Canova, G. (1996). Viscoplastic modeling of texture development in polycrystalline ice with a self-consistent approach: Comparison with bound estimates. *Journal of Geophysical Research*, *101*(B6), 13851–13868. https://doi.org/10.1029/96jb00412

Chib, S., & Greenberg, E. (1995). Understanding the metropolis-Hastings algorithm. *The American Statistician*, *49*(4), 327–335. https://doi.org/10.2307/2684568

Crampin, S., & Lovell, J. H. (1991). A decade of shear-wave splitting in the Earth's crust: What does it mean? What use can we make of it? And what should we do next? *Geophysical Journal International*, *107*(3), 387–407. https://doi.org/10.1111/j.1365-246X.1991.tb01401.x

Doake, C. S. M., Frolich, R. M., Mantripp, D. R., Smith, A. M., & Vaughan, D. G. (1987). Glaciological studies on Rutford ice stream, Antarctica. *Journal of Geophysical Research*, *92*(B9), 8951–8960. https://doi.org/10.1029/jb092ib09p08951

Duval, P., Ashby, M. F., & Anderman, I. (1983). Rate-controlling processes in the creep of polycrystalline ice. *Journal of Physical Chemistry*, *87*(21), 4066–4074. https://doi.org/10.1021/j100244a014

Fan, S., Hager, T. F., Prior, D. J., Cross, A. J., Goldsby, D. L., Qi, C., et al. (2020). Temperature and strain controls on ice deformation mechanisms: Insights from the microstructures of samples deformed to progressively higher strains at −10, −20 and −30°C. *The Cryosphere*, *14*(11), 3875–3905. https://doi.org/10.5194/tc-14-3875-2020

Faria, S. H., Weikusat, I., & Azuma, N. (2014a). The microstructure of polar ice. Part I: Highlights from ice core research. *Journal of Structural Geology*, *61*, 2–20. https://doi.org/10.1016/j.jsg.2013.09.010

Faria, S. H., Weikusat, I., & Azuma, N. (2014b). The microstructure of polar ice. Part II: State of the art. *Journal of Structural Geology*, *61*, 21–49. https://doi.org/10.1016/j.jsg.2013.11.003

Gagliardini, O., Gillet-Chaulet, F., & Montagnat, M. (2009). A review of anisotropic polar ice models: From crystal to ice-sheet flow models. *Low Temperature Science*, *68*.

Gagliardini, O., Zwinger, T., Gillet-Chaulet, F., Durand, G., Favier, L., De Fleurian, B., et al. (2013). Capabilities and performance of Elmer/Ice, a new-generation ice sheet model. *Geoscientific Model Development*, *6*(4), 1299–1318. https://doi.org/10.5194/gmd-6-1299-2013

Gillet-Chaulet, F., Gagliardini, O., Meyssonnier, J., Zwinger, T., & Ruokolainen, J. (2006). Flow-induced anisotropy in polar ice and related ice-sheet flow modelling. *Journal of Non-Newtonian Fluid Mechanics*, *134*(1–3), 33–43. https://doi.org/10.1016/j.jnnfm.2005.11.005

Graham, F. S., Morlighem, M., Warner, R. C., & Treverrow, A. (2018). Implementing an empirical scalar constitutive relation for ice with flow-induced polycrystalline anisotropy in large-scale ice sheet models. *The Cryosphere*, *12*(3), 1047–1067. https://doi.org/10.5194/tc-12-1047-2018

Gudmundsson, G. H., & Jenkins, A. (2009). Ice-flow velocities on Rutford Ice Stream, West Antarctica, are stable over decadal timescales. *Journal of Glaciology*, *55*(190), 339–344. https://doi.org/10.3189/002214309788608697

Harland, S. R., Kendall, J. M., Stuart, G. W., Lloyd, G. E., Baird, A. F., Smith, A. M., et al. (2013). Deformation in Rutford ice stream, west Antarctica: Measuring shear-wave anisotropy from icequakes. *Annals of Glaciology*, *54*(64), 105–114. https://doi.org/10.3189/2013AoG64A033

Hill, R. (1952). The elastic behaviour of a crystalline aggregate. *Proceedings of the Physical Society Section A*, *65*(5), 349–354. https://doi.org/10.1088/0370-1298/65/5/307

IPCC. (2021). In V. Masson-Delmotte, P. Zhai, A. Pirani, S. L. Connors, C. Péan, et al. (Eds.), *Climate change 2021: The physical science basis. Contribution of working group I to the Sixth assessment report of the intergovernmental panel on climate change*. Cambridge University Press. https://doi.org/10.1017/9781009157896

Jordan, T. M., Besson, D. Z., Kravchenko, I., Latif, U., Madison, B., Nokikov, A., & Shultz, A. (2020). Modeling ice birefringence and oblique radio wave propagation for neutrino detection at the South Pole. *Annals of Glaciology*, *61*(81), 84–91. https://doi.org/10.1017/aog.2020.18

Jordan, T. M., Martín, C., Brisbourne, A. M., Schroeder, D. M., & Smith, A. M. (2022). Radar characterization of ice crystal orientation fabric and anisotropic viscosity within an Antarctic ice stream. *Journal of Geophysical Research: Earth Surface*, *127*(6), e2022JF006673. https://doi.org/10.1029/2022JF006673

King, E. C., Pritchard, H. D., & Smith, A. M. (2016). Subglacial landforms beneath Rutford ice stream, Antarctica: Detailed bed topography from ice-penetrating radar. *Earth System Science Data*, *8*(1), 151–158. https://doi.org/10.5194/essd-8-151-2016

Kufner, S. K., Brisbourne, A., Smith, A., Wookey, J., Martin, C., Hudson, T., & Kendall, J. M. (2022). *Shear wave splitting catalogue, Rutford ice stream (west Antarctica), November 2018 to February 2019 (version 1.0)*. UK Polar Data Centre. https://doi.org/10.5285/6FCC17AD-425B-4367-BD23-C4133A38E359

Kufner, S. K., Brisbourne, A. M., Smith, A. M., Hudson, T. S., Murray, T., Schlegel, R., et al. (2021). Not all icequakes are created equal: Basal icequakes suggest diverse bed deformation mechanisms at Rutford ice stream, West Antarctica. *Journal of Geophysical Research: Earth Surface*, *126*(3). https://doi.org/10.1029/2020JF006001

Lutz, F., Eccles, J., Prior, D. J., Craw, L., Fan, S., Hulbe, C., et al. (2020). Constraining ice shelf anisotropy using shear wave splitting measurements from active-source borehole seismics. *Journal of Geophysical Research: Earth Surface*, *125*(9), e2020JF005707. https://doi.org/10.1029/2020JF005707

Ma, Y., Gagliardini, O., Ritz, C., Gillet-Chaulet, F., Durand, G., & Montagnat, M. (2010). Enhancement factors for grounded ice and ice shelves inferred from an anisotropic ice-flow model. *Journal of Glaciology*, *56*(199), 805–812. https://doi.org/10.3189/002214310794457209

Martín, C., Gudmundsson, G. H., Pritchard, H. D., & Gagliardini, O. (2009). On the effects of anisotropic rheology on ice flow, internal structure, and the age-depth relationship at ice divides. *Journal of Geophysical Research*, *114*(4), F04001. https://doi.org/10.1029/2008JF001204

Maurel, A., Lund, F., & Montagnat, M. (2015). Propagation of elastic waves through textured polycrystals: Application to ice. *Proceedings of the Royal Society A: Mathematical, Physical & Engineering Sciences*, *471*, (2177). 20140988. https://doi.org/10.1098/rspa.2014.0988

Montagnat, M., Löwe, H., Calonne, N., Schneebeli, M., Matzl, M., & Jaggi, M. (2020). On the birth of structural and crystallographic fabric signals in polar snow: A case study from the EastGRIP snowpack. *Frontiers of Earth Science*, *8*, 365. https://doi.org/10.3389/feart.2020.00365

Paulssen, H. (2004). Crustal anisotropy in southern California from local earthquake data. *Geophysical Research Letters*, *31*(1), L01601. https://doi.org/10.1029/2003GL018654

Pettit, E. C., Thorsteinsson, T., Jacobson, H. P., & Waddington, E. D. (2007). The role of crystal fabric in flow near an ice divide. *Journal of Glaciology*, *53*(181), 277–288. https://doi.org/10.3189/172756507782202766

Picotti, S., Vuan, A., Carcione, J. M., Horgan, H. J., & Anandakrishnan, S. (2015). Anisotropy and crystalline fabric of Whillans ice stream (West Antarctica) inferred from multicomponent seismic data. *Journal of Geophysical Research: Solid Earth*, *120*(6), 4237–4262. https://doi.org/10.1002/2014JB011591

Qi, C., Prior, D. J., Craw, L., Fan, S., Llorens, M.-G., Griera, A., et al. (2019). Crystallographic preferred orientations of ice deformed in direct-shear experiments at low temperatures. *The Cryosphere*, *13*(1), 351–371. https://doi.org/10.5194/tc-13-351-2019

Reuss, A. (1929). Berechnung der Fließgrenze von Mischkristallen auf Grund der Plastizitätsbedingung für Einkristalle. In *Zeitschrift für Angewandte Mathematik und Mechanik* (Vol. 9, pp. 49–58). https://doi.org/10.1002/zamm.19290090104

Richards, D. H., Pegler, S. S., Piazolo, S., & Harlen, O. G. (2021). The evolution of ice fabrics: A continuum modelling approach validated against laboratory experiments. *Earth and Planetary Science Letters*, *556*, 116718. https://doi.org/10.1016/j.epsl.2020.116718

Savage, M. K., Wessel, A., Teanby, N. A., & Hurst, A. W. (2010). Automatic measurement of shear wave splitting and applications to time varying anisotropy at Mount Ruapehu volcano, New Zealand. *Journal of Geophysical Research*, *115*(12), B12321. https://doi.org/10.1029/2010JB007722

Savage, M. S. (1999). Seismic anisotropy and mantle deformation: What have we learned from shear wave splitting? *Reviews of Geophysics*, *37*(1), 65–106. https://doi.org/10.1029/98RG02075

Silver, P. G., & Chan, W. W. (1991). Shear wave splitting and subcontinental mantle deformation. *Journal of Geophysical Research*, *96*(B10), 16429. https://doi.org/10.1029/91jb00899

Silver, P. G., & Savage, M. K. (1994). The interpretation of shear-wave splitting parameters in the presence of two anisotropic layers. *Geophysical Journal International*, *119*(3), 949–963. https://doi.org/10.1111/j.1365-246X.1994.tb04027.x

Smith, A. M., Anker, P. G. D., Nicholls, K. W., Makinson, K., Murray, T., Costas-Rios, S., et al. (2020). Ice stream subglacial access for ice sheet history and fast ice flow: The BEAMISH Project on Rutford Ice Stream, West Antarctica and initial results on basal conditions. *Annals of Glaciology*, *62*(85–86), 1–9. https://doi.org/10.1017/aog.2020.82

Smith, E. C., Baird, A. F., Kendall, J. M., Martín, C., White, R. S., Brisbourne, A. M., & Smith, A. M. (2017). Ice fabric in an Antarctic ice stream interpreted from seismic anisotropy. *Geophysical Research Letters*, *44*(8), 3710–3718. https://doi.org/10.1002/2016GL072093

Smith, E. C., Smith, A. M., White, R. S., Brisbourne, A. M., & Pritchard, H. D. (2015). Mapping the ice-bed interface characteristics of Rutford ice stream, West Antarctica, using microseismicity. *Journal of Geophysical Research: Earth Surface*, *120*(9), 1881–1894. https://doi.org/10.1002/2015JF003587

Stoll, N., Kerch, J., Kleitz, I., Eichler, J., Shigeyama, W., Homma, T., et al. (2018). An analysis of the influence of deformation and recrystallisation on microstructures of the EastGRIP ice core. In *The ninth symposium on polar science*. National Institute of Polar Research (NIPR).

Teanby, N. A., Kendall, J. M., & van der Baan, M. (2004). Automation of shear-wave splitting measurements using cluster analysis. *Bulletin of the Seismological Society of America*, *94*(2), 453–463. https://doi.org/10.1785/0120030123

USGS. (2007). *Landsat image mosaic of Antarctica (LIMA)*. U. S Geological Survey Fact. Sheet 2007–3116.

Voigt, W. (1887). In A. G. Wiss (Ed.), *Theoretische Studien über die Elasticitätsverhältnisse der Krystalle. I. Ableitung der Grundgleichungen aus der Annahme mit Polarität begabter Moleküle* (Vol. 34, pp. 3–52). (in German).

Walsh, E., Arnold, R., & Savage, M. K. (2013). Silver and Chan Revisited. *Journal of Geophysical Research: Solid Earth*, *118*(10), 5500–5515. https://doi.org/10.1002/jgrb.50386

Wookey, J. (2012). Direct probabilistic inversion of shear wave data for seismic anisotropy. *Geophysical Journal International*, *189*(2), 1025–1037. https://doi.org/10.1111/j.1365-246X.2012.05405.x